# Mobile Communications Base-station Array Antenna:

# Characterization of Environment

by

Trent McKeen

B.A.Sc., Simon Fraser University, 1993

THESIS SUBMITTED IS PARTIAL FULFILLMENT OF THE

REQUIREMENTS FOR THE DEGREE OF MASTER OF APPLIED SCIENCE

in the School of Engineering Science

© Trent McKeen 1995

SIMON FRASER UNIVERSITY

August, 1995

# APPROVAL

NAME: Trent McKeen

DEGREE: Master of Applied Science (Engineering Science)

TITLE OF THESIS: Mobile Communications Base-station Array Antenna: Characterization of Environment

EXAMINING COMMITTEE:

Chairman:

Dr. Paul Ho, P. Eng.
Associate Professor
School of Engineering Science, SFU

Senior Supervisor:

Dr. Shawn Stapleton, P.Eng.
Associate Professor
School of Engineering Science, SFU

Supervisor:

Dr. M. Parameswaran
Assistant Professor
School of Engineering Science, SFU

External Examiner:

Mr. Pete McConnell
Principle Engineer
Sierra Wireless Inc.

DATE APPROVED:

# PARTIAL COPYRIGHT LICENSE

I hereby grant to Simon Fraser University the right to lend my thesis, project or extended essay (the title of which is shown below) to users of the Simon Fraser University Library, and to make partial or single copies only for such users or in response to a request from the library of any other university, or other educational institution, on its own behalf or for one of its usrs. I further agree that permission for multiple copying of this work for scholarly purposes may be granted by me or the Dean of Graduate Studies. It is understood that copying or publication of this work for financial gain shall not be allowed without my written permission.

**Title of Thesis/Project/Extended Essay**

**"Mobile Communications Base-Station Array Antenna: Characterization of Environment"**

**Author:**

(signature)

_____

(name)

August 16, 1995
(date)

## Abstract

The demand for mobile telephone services is rapidly increasing while the frequencies allocated for this purpose have remained unchanged. In order to achieve higher user capacity, within the existing infrastructure, innovative system designs are being sought. Phased array base-station antennas have been proposed by many authors as a means of achieving higher spectral efficiency.

This paper examines the behavior of a phased array base-station antenna in a real urban environment. Field tests were performed to characterize the fading environment as seen by a multi-element base-station antenna. The primary goal of the field tests was to obtain the cross-correlation matrix for the different antenna elements. All the hardware designed and built for the field tests is documented, as well as the methods used to extract and compile the measured data.

As equipment for mobile phased array systems is developed, there will be a demand for a "spatial channel simulator" — a fading environment simulator which has the ability of simulating multi-element (directional) antennas. This paper also examines the development of a spatial channel simulator. It introduces the mathematical model used in its development as well as documents the hardware and software components of the system. Finally, the simulators performance is compared to true field test data. The results show that the statistical properties of the signals generated by the simulator very accurately duplicate those of signals encountered in the field.

# ACKNOWLEDGMENTS

# Contents

# List of Figures

# Chapter 1

# introduction

## 1.1    Synopsis of Chapter

This thesis documents two related topics.

1. The construction of a phased array antenna where the phase adjustments are done at baseband using a digital signal processor (DSP).

2. The construction of a spatial channel simulator – a fading channel simulator used on multiple element antenna arrays.

This chapter discusses the background of both the phased array antenna and the spatial channel simulator.

## 1.2    Phased Array Antennas

The general concept of phased array antennas dates back many years. A phased array system consists of a number of radiating elements who's relative phases are adjustable through the use of ferrite phase

shifters. Any recent work related to the topic of phased array antennas has been done in the area of enhanced performance of the RF phase tuning ferrites and steering algorithms.

Dr. Shawn Stapleton[13], has proposed a different approach to the phased array antenna. With this approach, the antenna array is the same, except there are no longer any RF phase tuning ferrites. Instead, each antenna element is individually downconverted to a complex baseband signal. Digital signal processing is then used to steer the beam, track a signal, provide angle diversity etc. See [13] for a more detailed description of the system.

The advantages a phased array antenna provide when used as the base-station antenna in a cellular network have been well documented. However, a base band steerable, phased array antenna has advantages over the existing phased array antenna technology in such situations. The baseband phased adjusted array can simultaneously track multiple signals simply by computationally combining the baseband signals differently. With the existing phased array technology, one could hop from one signal to another, but it is not possible to simultaneously maintain two or more channels. If phased array technology is to be used in cellular radio, the ability to maintain multiple channels is a must. Consider this example. Suppose there were two mobile vehicles in a given cell. One at $+10^o$ and the other at $-10^o$ relative to boresight. Vehicle 1 is transmitting on channel 1 while vehicle 2 is transmitting on channel 2. A traditional phased array antenna could only steer the beam in the direction of one of the vehicles because the phase adjustments are done at RF. With a baseband phase adjusted array, the system could simultaneously steer the beam in two different directions and provide techniques such as phase diversity to both vehicles simply because the phase adjustments are done at baseband, in real time, using a DSP.

This paper examines the performance of a baseband phase adjusted array. A complete system consisting of a seven element antenna array, seven complex baseband receivers and a digital signal processor was constructed and its performance evaluated in the field.

## 1.3  Spatial Channel Simulators

Spatial channel simulators are an extension of an old concept – the fading channel simulator. A fading channel simulator is used to mimic the fading environment and permits easy testing of mobile receivers without performing field tests. Fading channel simulators have been around for a number of years and all tend to employ very similar architecture in their design [1] [2] [3] [5] [6]. Because of increasing interest in utilizing phased array antennas in a mobile environment, there has been a growing interest in a new type of simulator, a spatial channel simulator.

A fading channel simulator is used to simulate multipath fading that an omni-directional antenna might see as it passes through a fading environment; like a cellular radio user might observe as he walks down a street surrounded by many RF scattering objects such as buildings, cars and people. On the other hand, a spatial channel simulator is used to simulate the environment a mobile base-station might see. The base-station may be listening to a mobile unit which is in a fading environment much like the one just described, but the base-station antenna itself is typically free of any significant local scatterers. The base-station antenna will see a fading signal due to the fading environment at the mobile, but there is no significant local standing wave pattern set up around the base-station antenna. As a result, the different elements of the phased array antenna, provided they are closely spaced, receive highly correlated signals.

Despite the significant differences in the two models just described, a fading channel simulator and the spatial channel simulator employ very similar architectures. The spatial channel simulator was a collection of $N$ fading channel simulators, where $N$ was the number of elements in the antenna array. A single, non-fading, signal fed the spatial channel simulator and the simulator output $N$, RF fading signals. Each of the $N$ RF signals were phase shifted relative to one another to simulate the effect of a receive signal incident on the array at an arbitrary angle off boresight, giving the spatial characteristics. In addition, the spatial channel simulator recreated the effect of non-ideal correlation between elements of a phase array antenna.

The spatial channel simulator discussed in this thesis utilizes DSP control which provided superior single

channel performance to that of a typical fading channel simulator. Spectral shaping through digital filtering was much superior to the analog techniques employed in most fading channel simulators.

This paper discusses the design of the spatial channel simulator. All the hardware and software is documented as well as the performance of the prototype.

# Chapter 2

# multipath interference

## 2.1 Synopsis of Chapter

Nature is seldom kind. One of the most common uses for radio communication systems is to communicate with people on the move. Unfortunately, mobile communication is complicated by some unique and difficult transmission problems. A radio signal transmitted between a fixed base-station and a vehicle moving in a typical urban environment exhibits severe variations in both amplitude and frequency. Fades of up to 40dB below the mean are common with successive minima occurring about a half wavelength apart (17cm @ 850MHz). A vehicle traveling through this fading environment can experience random signal fluctuations occurring at rates of $10 - 100$Hz. The fading phenomena is due to multipath wave interference which arises from the scattering of radio waves by buildings and other structures in the vicinity of the mobile.

This chapter introduces the concept of Rayleigh fading by first discussing the standard Rayleigh fading model seen in most text books on the subject. It also presents a model for Rayleigh fading as seen by a multi-element base-station antenna.

## 2.2 Standard Rayleigh Fading Model

### 2.2.1 The Mathematical Model

The standard fading model assumes a transmission path starting at the base-station and ending at the mobile unit. A diagram of this simple model is shown in Figure 2.1. As the vehicle moves with a velocity $v$, the motion introduces a Doppler shift in every wave:

$$\omega_n = \beta v \cos(\alpha_n) \tag{2.1}$$

where $\beta = \frac{2\pi}{\lambda}$.
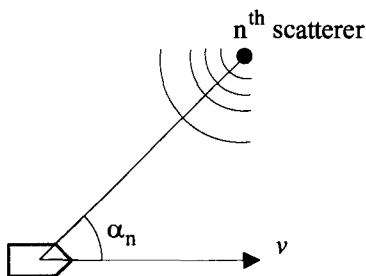


Figure 2.1: Rayleigh Fading Model

The complete received signal is therefore the sum of the $N$ individual scattered components.

$$E_z = E_0 \sum_{n=1}^{N} C_n \cos(\omega_c t + \omega_n t + \phi_n) \tag{2.2}$$

where $\omega_c$ is the carrier frequency, $E_0 C_n$ is the amplitude of the $n^{th}$ wave, and $\phi_n$ are the random phase angles uniformly distributed from 0 to $2\pi$.

The $C_n$'s have been normalized so that the average across the ensemble is

$$E\left\{C_n^2\right\} = 1 \tag{2.3}$$

For large values of $N$, the central limit theorem suggests that $E_z$ is approximately a Gaussian random process. Decomposing $E_z$ into its in-phase and quadrature components results in

$$E_z = I(t)\cos(\omega_c t) - Q(t)\sin(\omega_c t) \tag{2.4}$$

where

$$I(t) = E_0 \sum_{n=1}^{N} C_n \cos(\omega_n t + \phi_n) \tag{2.5}$$

$$Q(t) = E_0 \sum_{n=1}^{N} C_n \sin(\omega_n t + \phi_n) \tag{2.6}$$

$I(t)$ and $Q(t)$ are also Gaussian random processes with zero mean and equal variance.

$$E\left\{I(t)^2\right\} = E\left\{Q(t)^2\right\} = \frac{E_0^2}{2} = E\left\{|E_z|^2\right\} \tag{2.7}$$

Another important property of $I(t)$ and $Q(t)$ is that they are uncorrelated (and therefore independent).

$$E\left\{I(t)Q(t)\right\} = 0 \tag{2.8}$$

Because $I(t)$ and $Q(t)$ are Gaussian, their probability density functions are given by

$$p(x) = \frac{1}{\sqrt{2\pi b}} e^{-x^2/2b} \tag{2.9}$$

where $b = \frac{E_0^2}{2}$ is the mean power.

The envelope of $E_z$ is given by

$$r = \left(I(t)^2 + Q(t)^2\right)^{\frac{1}{2}} \tag{2.10}$$

which has a Rayleigh pdf given by

$$p(r) = \begin{cases} \frac{r}{b} e^{-r^2/2b} & r \geq 0 \\ \\ 0 & r < 0 \end{cases} \tag{2.11}$$

The phase of $E_z$ is uniform between 0 and $2\pi$.

Both the Gaussian and Rayleigh distributions are shown in Figure 2.2.
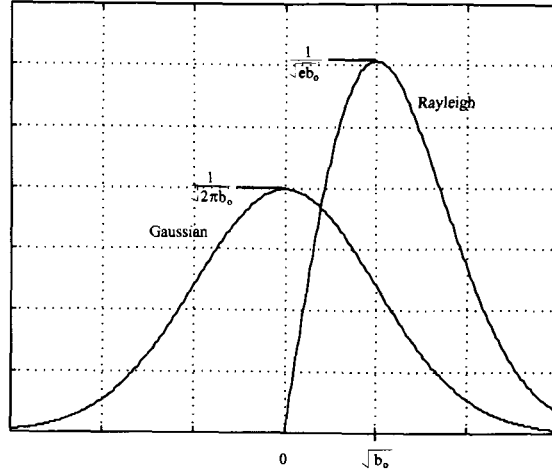
Figure 2.2: Rayleigh, Gaussian Distributions

## 2.2.2 Power Spectra of the Fading Signal

As before, we assume that the field consists of $N$ independent waves which are summed to give the total field at the receiver. As $N \to \infty$, the incident power included in an angle between $\alpha$ and $\alpha + d\alpha$ will approach a continuous instead of discrete distribution. It is usually assumed that the distribution of incident power with arrival angle is uniform. As a result, the fraction of the total incident power in a small angle, $d\alpha$, is

$$p(\alpha) = \frac{1}{2\pi} \, d\alpha \tag{2.12}$$

Equation 2.12 represents the differential variation of received power with angle. It is possible to find the field spectra, $S(f)$, by equating equation 2.12 to the differential variation of received power with frequency.

$$S(f) \, |df| = b \left[ p(\alpha) + p(-\alpha) \right] \, |d\alpha| \tag{2.13}$$

where $b$ is the average power that would be received by an isotropic antenna.

8

First we must note the relationship between frequency and angle expressed in equation 2.1.

$$f(\alpha) = f_m \cos(\alpha) + f_c \qquad (2.14)$$

$$
\begin{aligned}
|df| &= f_m \left| -\sin(\alpha) \right| |d\alpha| \\
&= \sqrt{f_m^2 - (f - f_c)^2} \, |d\alpha| \qquad (2.15)
\end{aligned}
$$

where $f_m = \frac{\beta v}{2\pi} = \frac{v}{\lambda}$, is the maximum Doppler shift and $f_c$ is the carrier frequency.

Equation 2.13 now gives

$$S(f) = \frac{b}{\pi f_m} \left[ 1 - \left( \frac{f - f_c}{f_m} \right)^2 \right]^{-\frac{1}{2}} \qquad (2.16)$$

### 2.2.3 Level Crossing Rate and Duration of Fades

The level crossing rate and the average duration of fades are two important and easily measured characteristics of a fading signal. The derivation of these two parameters is documented by Jakes[7]. Only their expressions are given here.

The level crossing rate, $N_R$, is defined as the expected rate at which the signal's envelope crosses a specified level, $R$, in the positive direction.

$$N_R = \sqrt{2\pi} \, f_m \rho e^{-\rho^2} \qquad (2.17)$$

where $\rho = \frac{R}{R_{RMS}}$.

The average duration of fades, $\overline{\tau}$, is defined as the average time the fading signal's envelope remains below a specified level, $R$. It is given by

$$\overline{\tau} = \frac{e^{\rho^2} - 1}{\rho f_m \sqrt{2\pi}} \qquad (2.18)$$

## 2.2.4 A Fading Channel Simulator

Laboratory simulation of multipath interference is an attractive alternative to performing field tests. There are a couple of methods for duplicating the signals encountered in the field, but the one used in this investigation involved quadrature amplitude modulation. A block diagram of a fading channel simulator can be seen in Figure 2.3.
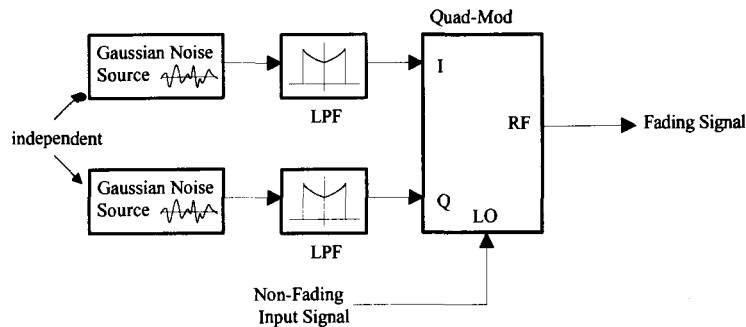
Figure 2.3: Fading Channel Simulator Block Diagram

Its development follows directly from the mathematical model derived earlier where two independent random Gaussian processes, $I(t)$ and $Q(t)$, which represent the in-phase and quadrature component of the fading signal, are used to modulate the carrier signal. The low pass filters shown in Figure 2.3 are used to shape the same power spectrum of the $I(t)$ and $Q(t)$ signals. The resulting RF power spectrum will then be identical to that of $I(t)$ and $Q(t)$.

# 2.3 Directional Antenna Rayleigh Fading Model

The results of the previous section were obtained by considering the mobile unit as the receiver. The model presented here assumes the transmission path originates at the mobile unit and ends at the base-station. At first thought, it might seem that transmission from the mobile to the base-station should not change matters. Radio transmission in a linear medium obeys the reciprocity theorem. However, the reciprocity

theorem must be applied with care in a scattering medium. In a typical mobile communications system, the base-station is positioned on top of a high building with no scatterers in the immediate vicinity. On the other hand, the mobile is positioned on the ground with a number of scatterers within a relatively small distance of the mobile. If the mobile is the receiver, it receives a number of signals from all different directions ($360^o$ around the mobile). However, if the base-station is considered as the receiver, the signals all arrive at the receiver from more or less one direction. This model also differs from the previous one in that the receiving antenna consists of a number of receiving elements – the antenna is directional.

## 2.3.1    Mathematical Model

This section discusses the model for the base-station fading environment. The model assumes a ring of scatterers which form a circle of radius $r$ surrounding the mobile. This model, as outlined by Jakes[7], considers the scatterers fixed while the mobile moves an incremental distance, $dx$, inside the ring of scatterers. Figure 2.4(a) shows the geometry of the situation. This model is useful for calculating the spectrum and correlation functions at the base-station and is widely accepted in the academic community.
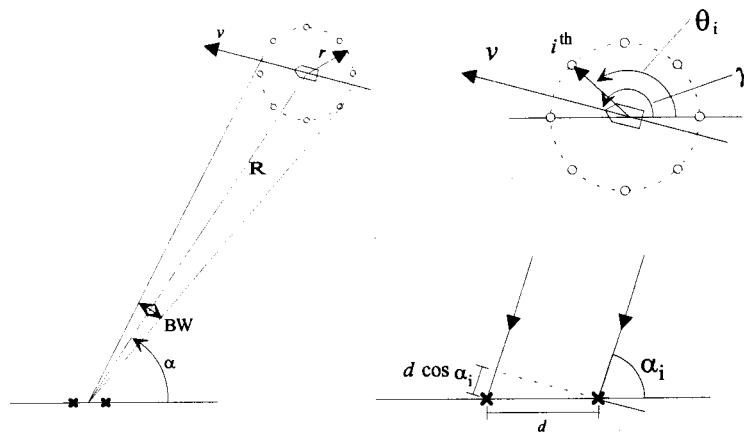


Figure 2.4: Fading Model

The distance, $R$, from the base-station to the mobile is assumed to be much greater than $r$. This assures that the waves reflecting from each of the $N$ scatterers are essentially parallel once they reach the antenna.

Under these conditions, the baseband equivalent signal at the individual antenna elements is given by

$$
\begin{aligned}
E_1 &= \sum_{i=1}^{N} C_i\, e^{j\,\phi_i(t)} \\
E_2 &= \sum_{i=1}^{N} C_i\, e^{j\,\phi_i(t) - \beta d \cos(\alpha_i)} \\
E_3 &= \sum_{i=1}^{N} C_i\, e^{j\,\phi_i(t) - 2\beta d \cos(\alpha_i)} \\
&\ldots etc.
\end{aligned}
\tag{2.19}
$$

The in-phase and quadrature phase components are given by,

$$
\begin{aligned}
I_1 &= \sum_{i=1}^{N} C_i \cos\left(\phi_i(t)\right) & Q_1 &= \sum_{i=1}^{N} C_i \sin\left(\phi_i(t)\right) \\
I_2 &= \sum_{i=1}^{N} C_i \cos\left(\phi_i(t) - \beta d \cos(\alpha_i)\right) & Q_2 &= \sum_{i=1}^{N} C_i \sin\left(\phi_i(t) - \beta d \cos(\alpha_i)\right) \\
I_3 &= \sum_{i=1}^{N} C_i \cos\left(\phi_i(t) - 2\beta d \cos(\alpha_i)\right) & Q_3 &= \sum_{i=1}^{N} C_i \sin\left(\phi_i(t) - 2\beta d \cos(\alpha_i)\right)
\end{aligned}
\tag{2.20}
$$

$$\ldots etc.$$

where

$$\phi_i = -\beta v t \cos(\alpha_i - \gamma) - \frac{r}{c}\omega_c \cos(\theta_i - \alpha_i)$$

$C_i$      Amplitude of the wave reflected by the $i^{th}$ scatterer.

$\omega_c$      Radian frequency of carrier equals $2\pi f_c$.

$\beta$      Wave number equals $2\pi/\lambda$.

$d$      Antenna spacing.

$v$      Velocity of the mobile unit.

$\gamma$      Angle that indicates the direction of travel.

$r$      Radius to the surrounding scatterers.

$c$      Speed of light.

$\theta_i$      Angle that indicates the direction from the mobile to the $i^{th}$ scatterer.

$\alpha_i$      Angle at which the incoming wave arrives at the base-station receiver.

$$N \qquad \text{Number of scatterers.}$$

$$\beta vt \cos(\alpha_i - \gamma) \qquad \text{Contribution by the Doppler effect.}$$

$$\frac{r}{c}\omega_c \cos(\theta_i - \alpha_i) \qquad \text{Contribution by the range delay.}$$

If the same procedure used in section 2.2.2 is used to find the frequency spectrum, we see the two models give the same result because $\frac{|df|}{|d\alpha|}$ is the same in both cases. In fact, the spectrum is the same as that derived in section 2.2.2.

$$S(f) = \frac{b}{\pi f_m}\left[1 - \left(\frac{f - f_c}{f_m}\right)^2\right]^{-\frac{1}{2}} \tag{2.21}$$

Another important property of the fading environment when a multi-element base-station antenna is used is the correlation of received signal based on space separation. Following Lee[9], if two random signals $r_1$ and $r_2$ are present where

$$r_1(t) = \sqrt{X^2(t) + Y^2(t)} = \sqrt{X_1^2 + Y_1^2} \tag{2.22}$$

and

$$r_2(t) = \sqrt{X^2(t + \tau) + Y^2(t + \tau)} = \sqrt{X_2^2 + Y_2^2} \tag{2.23}$$

Then, the normalized correlation function is

$$\rho_{12}(\tau) = \frac{(E[X_1 X_2])^2 + (E[X_1 Y_2])^2}{(E[X_1^2])^2} \tag{2.24}$$

provided

$$\left.\begin{array}{l} E[X_m^2] = E[Y_m^2] \\ E[X_m] = E[Y_m] = 0 \end{array}\right\} m = 1, 2 \tag{2.25}$$

## 2.3.2 The Spatial Channel Simulator

When testing directional antennas it is again more convenient to perform laboratory simulations than actual field tests. A simulator which can simulate the fading characteristics observed by a directional antenna is called a "spatial channel simulator" because the directional characteristics of the antenna make knowledge of the spatial geometry of the problem necessary. For a simple fading channel simulator, the

mobiles distance from the base-station, $R$, is the only parameter needed. And if log-normal fading is being ignored, even this parameter can be eliminated from the simulation. With a spatial channel simulator, both the distance to the mobile and the angle of the mobile, $\alpha$, must be known. This extra knowledge allows the simulation of Rayleigh fading as well as log-normal fading and co-channel interference.

The design of a spatial channel simulator basically involves production of $M$ fading channel simulators, where $M$ is the number of elements in the receiving antenna array. In our case, $M = 7$. Figure 3.2 shows the block diagram of a spatial channel simulator. The mathematical model (Eq. 2.19) suggests that the only difference between the signal received by any of the 7 elements is an incremental phase offset given by $\beta d \cos(\alpha_i)$. However, Eq. 2.24 shows that the signals received at the 7 different antenna elements are not 100% correlated. In fact they have a cross-correlation matrix given by $\boldsymbol{\Sigma}_Y$, where $\boldsymbol{\Sigma}_Y$ is defined as

$$
\boldsymbol{\Sigma}_Y = \begin{bmatrix}
\rho_{11} & \rho_{12} & \rho_{13} & \rho_{14} & \rho_{15} & \rho_{16} & \rho_{17} \\
\rho_{21} & \rho_{22} & \rho_{23} & \rho_{24} & \rho_{25} & \rho_{26} & \rho_{27} \\
\rho_{31} & \rho_{32} & \rho_{33} & \rho_{34} & \rho_{35} & \rho_{36} & \rho_{37} \\
\rho_{41} & \rho_{42} & \rho_{43} & \rho_{44} & \rho_{45} & \rho_{46} & \rho_{47} \\
\rho_{51} & \rho_{52} & \rho_{53} & \rho_{54} & \rho_{55} & \rho_{56} & \rho_{57} \\
\rho_{61} & \rho_{62} & \rho_{63} & \rho_{64} & \rho_{65} & \rho_{66} & \rho_{67} \\
\rho_{71} & \rho_{72} & \rho_{73} & \rho_{74} & \rho_{75} & \rho_{76} & \rho_{77}
\end{bmatrix}
\tag{2.26}
$$

and $\rho_{mn}$ is the correlation between the $m^{th}$ and $n^{th}$ antenna elements as defined in Eq. 2.24.

The spatial channel simulator must generate 14 independent Gaussian random variables. From these 14 random variables, 14 new variables, $I_1, \ldots, I_7$ and $Q_1, \ldots, Q_7$, can be obtained which have a cross-correlation matrix given by $\boldsymbol{\Sigma}_Y$.

Once the 7 random $I_m$ variables and the 7 random $Q_m$ variables have been generated with the desired cross-correlation, it is a simple matter to phase adjust $I_2 - I_7$ and $Q_2 - Q_7$ to produce the desired complex signals $I_1', \ldots, I_7'$ and $Q_1', \ldots, Q_7'$.

# Chapter 3

# spatial channel simulator

## 3.1  Synopsis of Chapter

This chapter outlines the design specifications and the functional specifications of the spatial channel simulator. The chapter is broken into four sections with each section discussing one of the four major blocks of the system. The four different sections are the following,

- The DSP

- The 14 channel D/A converter

- The reconstruction filter block(s)

- The Quadrature modulator(s)

## 3.2  General Considerations

A complete and accurate spatial channel simulator must be able to reproduce all the effects of a multipath fading environment. The spatial channel simulator discussed in this report was an initial attempt at

15

designing an accurate environment simulator. It was; however, simplified in a number of ways to speed up its completion, but still provide a proof of concept. The simulator reproduces the major features of a fading environment but does not recreate the following:

- The spatial channel simulator developed for this project, like most simulators, ignores the delay spread effect on the transmitted signal. Delay spread can only be accounted for using a number of expensive RF delay lines and summing their output. Also, delay spread only becomes noticeable as the bandwidth of the transmitted signal $B_s$ approaches the coherence bandwidth of the environment ($B_c = \frac{1}{2\pi\Delta}$ where $\Delta$ = delay spread). In our case $B_s = 5kHz << B_c = 636kHz$ (delay spread $\Delta = 0.25\mu s$).

- The simulator does not take into account co-channel interference. As a first attempt at producing a spatial channel simulator, co-channel interference was not considered. It can be incorporated by an extension of the present simulator by adding an additional directional noise source.

- The mobiles position was restricted to $\pm 20^o$ from boresight. The spatial channel simulator designed and discussed in this report is not a general purpose spatial channel simulator. This means it was designed to produce accurate multi-path environment simulations for the specific cellular system described by Dr. Shawn Stapleton[13]. The system described in reference [13] consists of a circular array of $K$ radiating elements equally spaced around a cylinder of radius $a$. At any one time, only $M$ elements out of $K$ are active forming a directional beam for each mobile user. The result is, the beam never has to steer very far from boresight while tracking a vehicle. If the vehicle ventures beyond some angular threshold $\phi$, the set of active elements is adjusted to bring the vehicle back to boresight. It is this feature which separates the spatial channel simulator discussed here from a truly general purpose spatial channel simulator. The simulator examined in this report makes the simplifying assumption that the beam never varies more that $\pm 20^o$ from boresight. For a general communications system, the simulator should allow for any vehicle position.

- The simulator does not recreate log-normal fading. Log-normal fading is a simple feature to include and unnecessarily complicated the analysis of the simulator.

The reason these features were not implemented was because they were conceptually very simple enhancements to the simulator, however they were very expensive in terms of the hardware requirements, software requirements and the time required to implement them.

The design of the spatial channel simulator basically involved the production of $M$ fading channel simulators, where $M$ was the number of elements in the receiving antenna array. In our case, $M = 7$. Equation 2.19 suggests that the only difference between the signal received by any of the 7 elements is an incremental phase offset given by $\beta d \cos(\alpha_i)$. However, equation 2.24 shows that the signals received at the 7 different antenna elements are not 100% correlated. In fact they have a cross-correlation matrix given by $\Sigma_Y$.

To make a point, the correlation coefficient versus antenna spacing for different arrival angles $\alpha$ and an incoming signal beamwidth of $3^o$ is shown in Figure 3.1(a). For the system proposed in this report, arrival angles were restricted to the range of $\alpha = 90^o \pm 20^o$ and the maximum distant between two antennas was $\frac{7\lambda}{2}$ (7 antennas spaced $\frac{\lambda}{2}$ apart). Under these restrictions, one can consider the correlation coefficients to be independent of arrival angle $\alpha$ and very close to 1.0 as seen in Figure 3.1(b).

Assuming the correlation coefficients to be independent of arrival angle $\alpha$ greatly simplifies the analysis. The correlation between different elements of the array can be described by a single cross-correlation matrix whose elements are independent of the vehicles position and therefore independent of time.

The design of the spatial channel simulator followed from the block diagram seen in Figure 3.2. The Gaussian noise sources, cross-correlation combiner algorithm, spectral shaping and phase adjustments were all done inside a TMS320C30 digital signal processor. The fourteen outputs ($I_1 - I_7$, $Q_1 - Q_7$) were output to a 14 channel D/A converter. The output of each D/A converter was connected to a tunable switched capacitor reconstruction filter. After the filter block, the seven $I$ and $Q$ pairs were applied to seven quadrature modulators to produce the seven fading signals. The system's three principal component
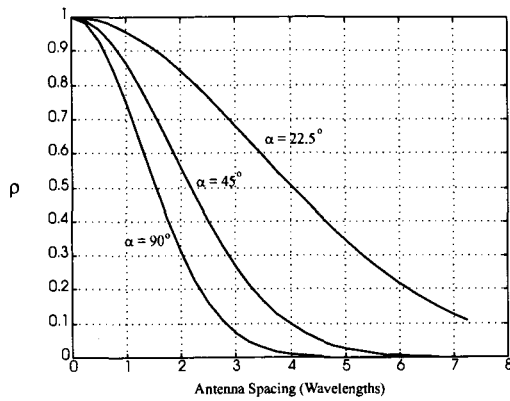
(a)
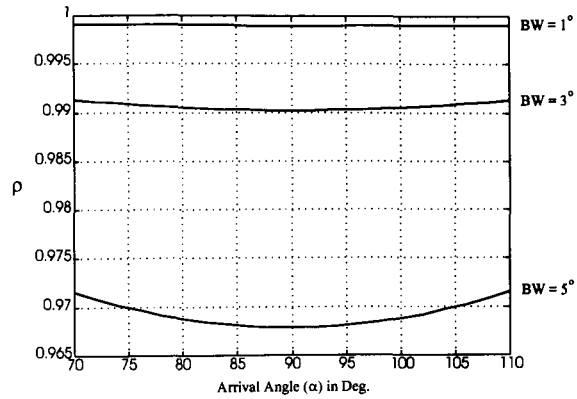
(b) Antenna Separation $= \frac{7\lambda}{2}$

Figure 3.1: Correlation Coefficients

are discussed separately in the following sections.

## 3.3  The DSP

The DSP device used was the TMS320C30. An IBM PC was equipped with a TMS320C30 evaluation board provided by Texas Instruments. The evaluation board allowed code for the C30 to be developed on the PC and then programmed into the evaluation board and run.

To ease the development, the code was written in 'C' and compiled using a 'C' compiler also supplied by Texas Instruments. The code generated by the 'C' compiler was far less efficient than code written in assembly, but it decreased the development time of the code significantly.

The DSP had four primary tasks which are pictorially represented in Figure 3.2 as the first four stages in the block diagram. The four primary tasks of the DSP were,

- the generation of Gaussian random samples

- combining the independent Gaussian samples to produce 7 $I$ and 7 $Q$ signals with a given cross-correlation matrix

18
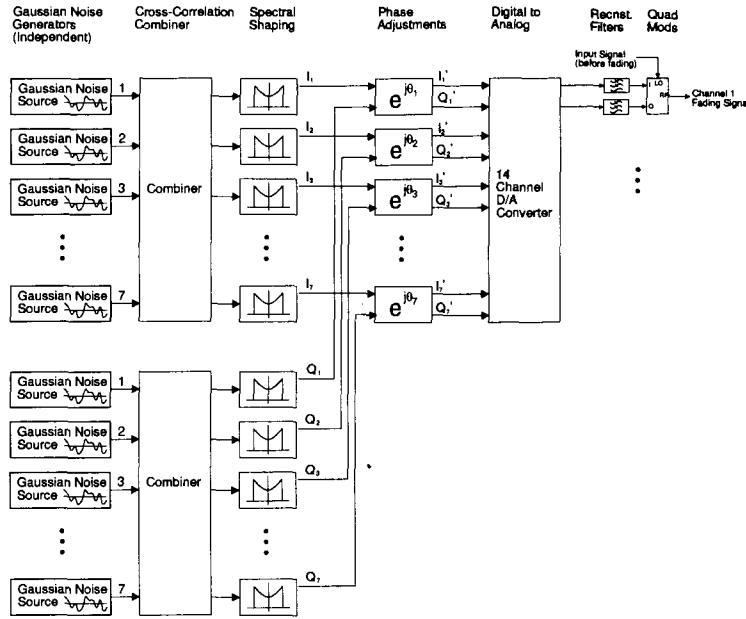
Figure 3.2: Spatial Channel Simulator Block Diagram

- spectral shaping through FIR filtering

- $I$ and $Q$ scaling to provide the necessary phase offsets between the antenna elements at RF.

How the DSP performed these tasks is discussed in the following four subsections.

### 3.3.1   Generation of Gaussian Random Samples

'C' has a built in random number generator. However, the 'C' supplied RAND function produces random numbers with a uniform distribution, but the simulator requires the generation of normally distributed numbers. To generate normally distributed random numbers, the DSP first generates a uniformly distributed random number and then performs a transformation on the number which results in a normally distributed number. The DSP used the RAND function to generate a random variable, $u$ which had a uniform distribution on the interval $[0, 1]$. With $u$, the DSP was then able to produce a random variable,

19

$r$, which had a Rayleigh distribution with variance $\sigma^2$ by applying the transformation,

$$r = \sigma\sqrt{-\ln(u)} \tag{3.1}$$

and another random variable, $\theta$, which was uniform on the interval $[0, 2\pi]$ according to the transformation,

$$\theta = 2\pi u \tag{3.2}$$

Finally, a random variable, $g$, was calculated which had a normal distribution with variance $\sigma^2$ according to the formula

$$g = r\cos(\theta) \tag{3.3}$$

The success of this algorithm depends on the success of the RAND function supplied with the 'C' compiler. Most random number generators are not that random. They usually have an auto-correlation different from the ideal $\delta(0)$. For time constraint reasons, no attempt was made to improve the "randomness" of the RAND function. The results shown in Section 4 suggest that the RAND function supplied with the 'C' compiler was adequate for the purpose of the simulator.

### 3.3.2   Gaussian Sample Combination Algorithm

Following the block diagram seen in Figure 3.2, after the DSP generated 7 independent Gaussian variables, it used them to construct 7 new random variables with the cross-correlation matrix shown in Figure 3.3.

This matrix was to come from the field test results discussed in Section 6.2. If you compare this matrix to those in Section 6.2, you will find that they do not match. The reason for this was, the cross-correlation matrix obtained from the field tests varied in time for reasons discussed in that section. As a result, a cross-correlation matrix at an arbitrary instant in time, and one which agrees with theory, was extracted from the field test measurements and used here as the desired cross-correlation matrix for the simulator.

The algorithm used by the DSP to construct the seven correlated variables from seven independent normally distributed variables is shown below.

20

$$\begin{bmatrix}
1.00 & 0.93 & 0.94 & 0.92 & 0.91 & 0.89 & 0.85 \\
0.93 & 1.00 & 0.95 & 0.93 & 0.90 & 0.86 & 0.78 \\
0.94 & 0.95 & 1.00 & 0.90 & 0.91 & 0.93 & 0.85 \\
0.92 & 0.93 & 0.90 & 1.00 & 0.96 & 0.94 & 0.90 \\
0.91 & 0.90 & 0.91 & 0.96 & 1.00 & 0.95 & 0.89 \\
0.89 & 0.86 & 0.93 & 0.94 & 0.95 & 1.00 & 0.94 \\
0.85 & 0.78 & 0.85 & 0.90 & 0.89 & 0.94 & 1.00
\end{bmatrix}$$

Figure 3.3: Programmed Cross-Correlation Matrix (both I and Q)

In general, if $\mathbf{A}$ is an $m \times m$ matrix, then

$$\mathbf{Y} = \mathbf{A}\mathbf{X} \tag{3.4}$$

is a m-variate Gaussian distribution with mean vector

$$\mu_Y = \mathbf{A}\mu_X \tag{3.5}$$

and covariance matrix

$$\Sigma_Y = \mathbf{A}\Sigma_X\mathbf{A}^T \tag{3.6}$$

In this particular case, $\mathbf{X}$ is 7-variate Gaussian with

$$\Sigma_X = \begin{bmatrix}
\sigma_1^2 & 0 & 0 & \cdots & 0 \\
0 & \sigma_2^2 & 0 & \cdots & 0 \\
0 & 0 & \sigma_3^2 & \cdots & 0 \\
\vdots & \vdots & \vdots & & \vdots \\
0 & 0 & 0 & \cdots & \sigma_7^2
\end{bmatrix} \tag{3.7}$$

Substituting this into equation 3.6, the resulting covariance of the combination process is then

$$\Sigma_Y = \sigma^2 \mathbf{A}\mathbf{A}^T \tag{3.8}$$

where

$$\sigma_1^2 = \sigma_2^2 = \sigma_3^2 = \cdots = \sigma^2 \tag{3.9}$$

Given the desired covariance matrix $\boldsymbol{\Sigma}_Y$ (or cross-correlation matrix $\rho_Y = \frac{\boldsymbol{\Sigma}_Y}{\sigma^2}$), $\mathbf{A}$ was determined. The combination algorithm then used equation 3.4 to generate the desired 7-variate Gaussian vector.

### 3.3.3 Spectral Shaping Through Finite Impulse Response (FIR) Filtering

Following the block diagram seen in Figure 3.2, after the DSP generated 7 correlated $I$ and $Q$ samples, it was necessary to filter the samples to shape their spectrum.

In Section 2.2.2 we developed an expression for the RF spectrum of the fading signal. The baseband equivalent of this spectrum is the following.

$$S(f) = \frac{b}{\pi f_m} \left[ 1 - \left( \frac{f}{f_m} \right)^2 \right]^{-\frac{1}{2}} \qquad (3.10)$$

Figure 3.4 shows a plot of the baseband spectrum.
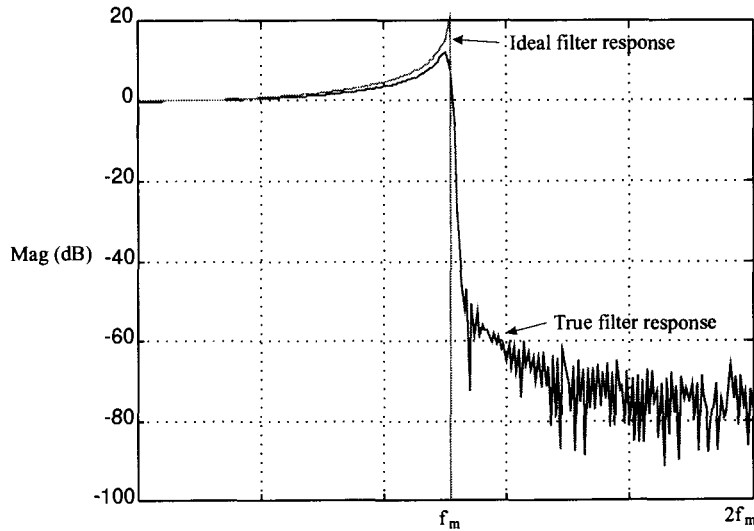


Figure 3.4: Spectral Shaping Filter Response

It was necessary for the DSP to shape the Gaussian noise according to this expression. However, there was a problem in that $f_m$ is a function of the mobiles velocity according to $f_m = \frac{v}{\lambda}$. To allow the DSP to simulate a number of different vehicle speeds, the corner frequency ($f_m$) of the filter had to be adjustable.

22

The obvious solution of recalculating filter coefficients each time a new filter (new velocity) was desired resulted in excessively long coefficient tables and poor resolution for filters with low cutoff frequencies. The alternative was to store a single filter table, but vary the rate at which the samples were output.

The filter spectrum shown in Figure 3.4 was the one used to generate the filter coefficients. The spectrum was defined up to $2f_m$. This meant the first image occurred at $4f_m$, but occupied the range of $3f_m$ to $5f_m$.

This method, while efficient in terms of the coefficient table, complicated the design of the reconstruction filter at the output of the digital to analog converter (DAC). So as to eliminate the images, the reconstruction filter had to pass $f_m$, but reject $3f_m$. $f_m$, unfortunately varied. It was therefore necessary to design a reconstruction filter which was tunable. See section 3.5 for details.

### 3.3.4  $I$ and $Q$ Phase Adjustments

Following the block diagram seen in Figure 3.2, once $I_1 - I_7$ and $Q_1 - Q_7$ were generated, they were adjusted to provide for the phase differences between channels due to the signal arrival angle, $\alpha$ (ie. $I'_1 - I'_7$ and $Q'_1 - Q'_7$ were calculated). A given $I$ and $Q$ can be scaled so as to keep the same signal magnitude ($\sqrt{I^2 + Q^2}$) but change its phase by $\theta$. The DSP calculated the $I$'s and $Q$'s according to

$$
\begin{aligned}
I'_1 &= I_1 & Q_1 &= Q \\
I'_2 &= I_2 \cos\theta - Q_2 \sin\theta & Q'_2 &= Q_2 \cos\theta + I_2 \sin\theta \\
I'_3 &= I_3 \cos 2\theta - Q_3 \sin 2\theta & Q'_3 &= Q_3 \cos 2\theta + I_3 \sin 2\theta
\end{aligned}
\tag{3.11}
$$

$$\ldots etc.$$

## 3.4   14 Channel D/A Converter

As seen in Figure 3.2 , after the DSP has computed the 7 $I$ samples and the 7 $Q$ samples, the samples were converted to an analog signal which was then used to modulate a carrier using a quadrature modulator.

The 14 channel D/A converter consisted of 14, 16-bit DACs and some address decoding so that each DAC could be written to individually. The DACs were double buffered. This allowed values to be written to each DAC sequentially, but a single clock to synchronize the "begin conversion" for all 14 DACs. If the 14 conversions were not initiated simultaneously, the spread in conversion times would introduce an additional phase offset which was a function of the instantaneous frequency of the signal. Initiating the conversions simultaneously ensured a predictable phase offset between channels which was controlled by the DSP through $I$ and $Q$ adjustments.

There were actually 16 ports available on the board. The first 14 ($P_0 - P_{13}$) correspond to the 14 DACs. The last 2 ($P_{14}$ and $P_{15}$) provide the common "begin conversion" control signals to the DACs.

The interface between the DSP and the 14 channel D/A converter was provided through the C30's extended bus. This bus occupied locations 002000 – 003000 of the C30. The 3 LSB address lines ($A_0 - A_2$) and the EXB signal (which signals an extended memory access) were decoded and used to control communications with the 16 ports on the board.

The schematics for the 14 channel DAC are shown in Figure 3.5 and 3.6. Figure 3.5 shows one channel of the 14 channel DAC. 14 of these circuits were constructed and combined with the controller circuit shown in Figure 3.6. The channel controller generated all the necessary enable signals for controlling the 14 different D/A channels as well as interfacing to the TMSC30 DSP board in the PC.

Figure 3.5: 14 Channel DAC – One channel
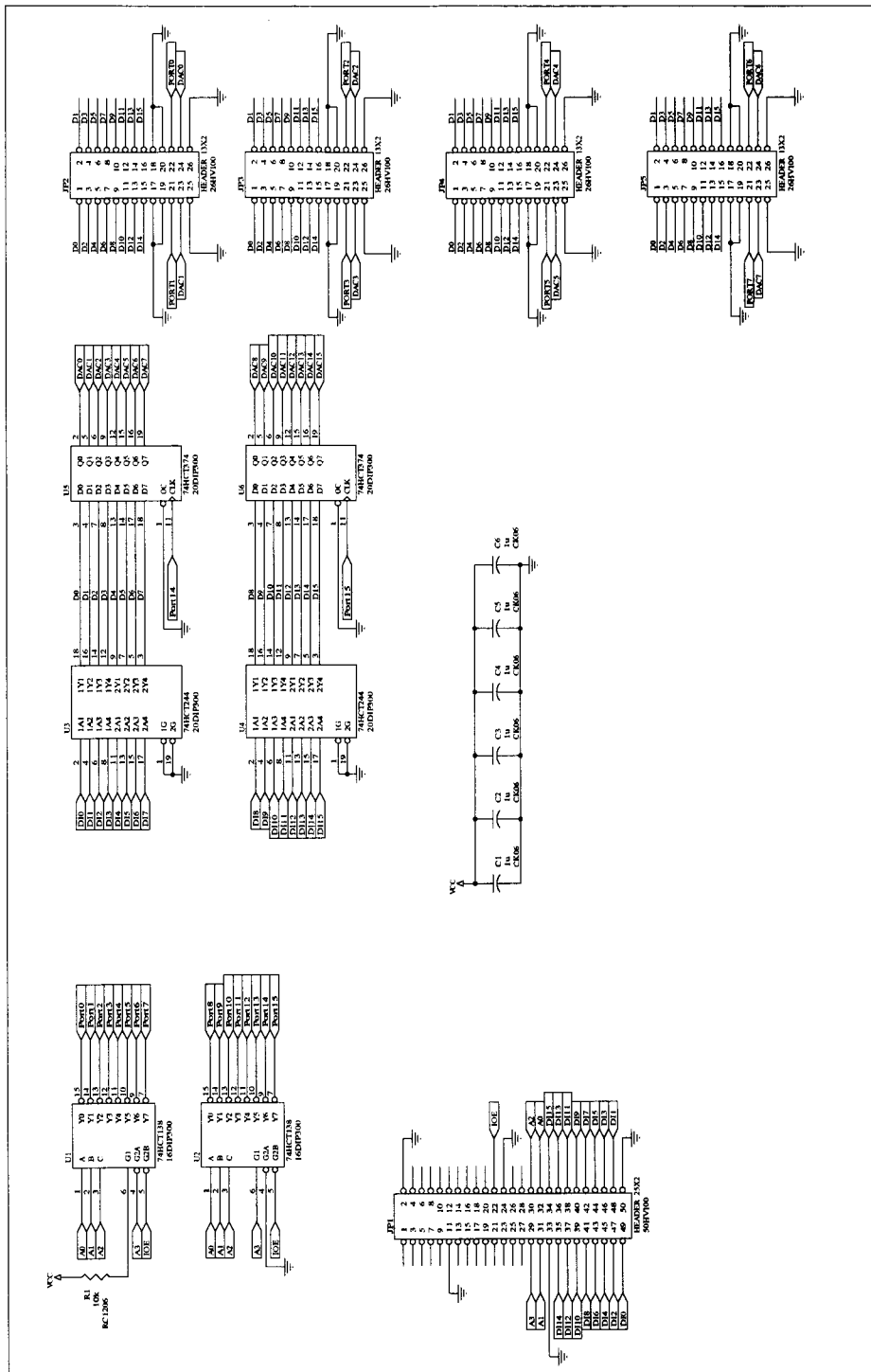
Figure 3.6: 14 Channel DAC – Channel Controller

## 3.5    Reconstruction Filter Block

The purpose of this block was to reject the spectral images produced by the DACs sampled output. Section 3.3 indicated that the first image appeared at $3f_m$. However, $f_m$ varied from 10Hz – 100Hz, corresponding to a velocity range of 12.5kph – 125kph at a carrier frequency of 860MHz. The variation of $f_m$ implied the image also varied over the range of 30Hz – 300Hz. The potential image at 30Hz was within the necessary pass band of the filter (10Hz – 100Hz). Therefore, the reconstruction filter had to be made tunable. The simplest way to provide an accurately tunable filter at low frequencies was the use of a switched capacitor filter (SCF). However, an SCF is also a "sampling" device. Fortunately, an SCF has a sampling divide ratio of 100:1 which meant the images created by the SCF would fall in the range of 300Hz – 3000Hz as its cutoff frequency was tuned over the necessary range of 30Hz – 300Hz. This allowed a fixed frequency filter to be used on the output of the SCF to eliminate the images produced by the SCF. The switched capacitor filter essentially moved the images into a range where they can be effectively filtered out.

The use of a switched capacitor filter also necessitated the use of an anti-aliasing filter on the input of the switched capacitor filter. Any spectrum above the clock rate of an SCF (300Hz to 3000Hz) is mirrored around the clock frequency. Potentially, power above 590Hz could fall back in-band. An anti-aliasing filter with a cutoff frequency of 150Hz was therefore included at the input of the switched capacitor filter.

A block diagram of a single reconstruction filter is shown in Figure 3.7 and the schematic for a single reconstruction filter is shown in Figure 3.8. This block was replicated 14 times, once for each of the 14 signals generated by the 14 channel DAC.

anti-aliasing filter (fc = 150Hz)   switched-cap filter (fc = 10 - 100Hz)   image reject filter (fc = 150Hz)   Quad-mod

$I_x$
(from 14ch DAC)

$Q_x$
(from 14ch DAC)

tuning CLK
(from DSP)

I

Q    LO

RF ──▶ Fading Signal

Non-fading Signal
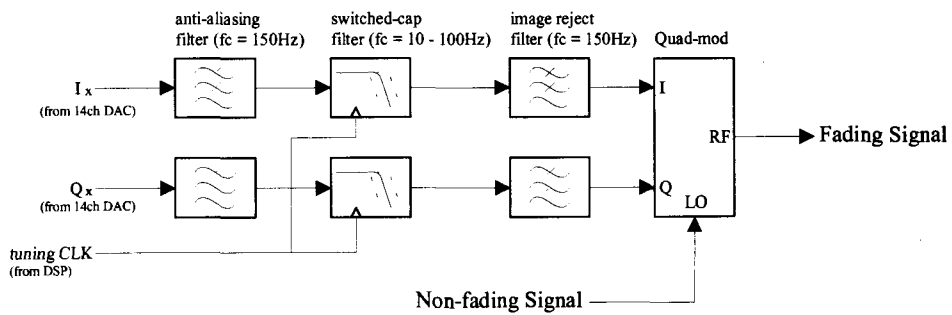
Figure 3.7: Reconstruction Filter Block Diagram
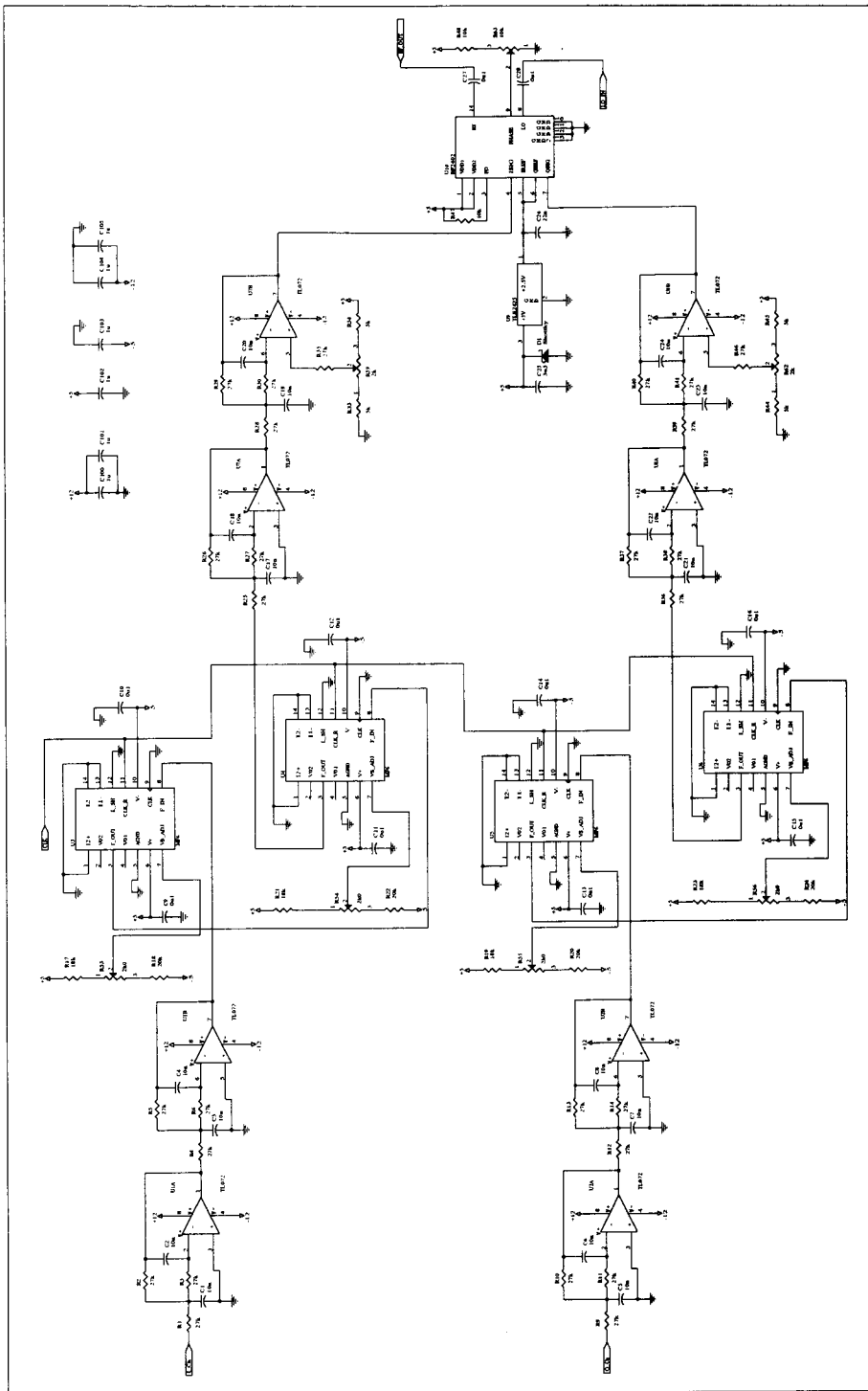
Figure 3.8: Switched Capacitor Filter and Anti-Aliasing Filters

## 3.6 Quadrature Modulator

The final stage on the simulator (see Figure 3.2) was the quadrature modulator (quad-mod). The function of the quad-mod was to generate an in-phase and quadrature phase carrier and AM modulate the two carriers with $I$ and $Q$ signals respectively. The two modulated signals were then summed to generate the output. The LO used to drive the quad-mod was the "test signal" that was to experience Rayleigh fading.

The quadrature modulator package used was the RF2402 by RF-Micro Devices. The schematic for the quad-mod section can also be seen in Figure 3.8.

There are a few factors which required special attention to ensure the quad-mod functioned properly. These were,

- The DC bias on both the $I$ and $Q$ modulating signals was important. If the DC bias on $I$ and $Q$ became unbalanced, the result was insufficient carrier suppression in the quad-mod. As a result, the DC bias on both the $I$ and $Q$ channels was made tunable through the use of a potentiometer (see Figure 3.8). The DC bias was also finely tuned by adjusting the offset values in the DSP.

- The phase error between the in-phase and quadrature phase carriers is critical. If the two carriers are not $90^0$ out of phase, the result is cross talk between the in-phase and quadrature phase channels. As a result, the phase offset between the two carriers was made tunable through the use of a potentiometer (see Figure 3.8).

- The relative AC levels between the $I$ and $Q$ channels is also important. This was adjusted so the AC levels on $I$ and $Q$ were the same at the input ports of the quad-mod by adjusting the DSP scaling.

# Chapter 4

# spatial channel simulator performance

## 4.1 Synopsis of Chapter

This chapter summarizes the measured performance of the spatial channel simulator. The analysis is divided into two sections. The first section looks at a single channel's performance. This includes all the single channels RF spectrum as well as envelope and phase distribution functions. The second section looks at the systems performance by examining the correlation statistics between different antennas.

## 4.2 The Measurement Process

The measurement techniques used to examine the performance of the spatial channel simulator were identical to those used to measure the performance of the phased array antenna in the field. The simulator was started and the seven simulator outputs were connected to the 7-channel receiver discussed

in Section 5.2.2. The base-band outputs of the receiver were then recorded and digitized as discussed in Section 5.2.4.

The following results were generated using MATLAB to process the digitized signals.

## 4.3 Single Channel Performance

### 4.3.1 Measured Probability Density Functions
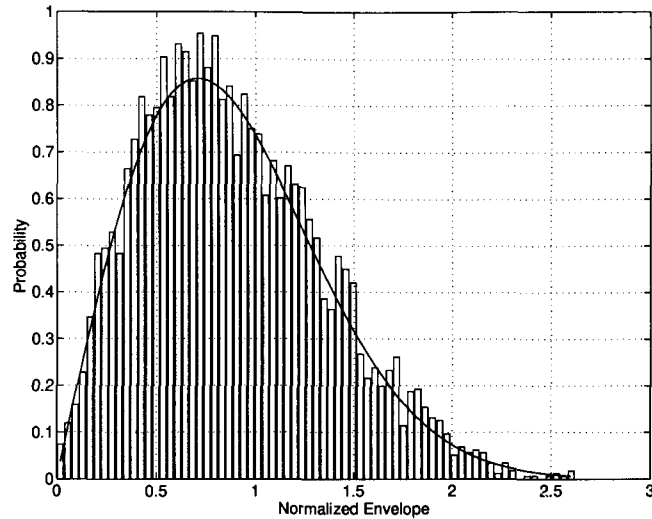


Figure 4.1: Simulated Envelope Distribution

The probability density functions were generated using 10 sec. worth of data. Both the envelope and phase distributions appear to be correct. It is impossible to prove that a set of data comes from a specific distribution because no practical amount of data can distinguish between two distributions which differ by only one part in $10^{10}$. And even such a small variation does not guarantee the data comes from a specific distribution.
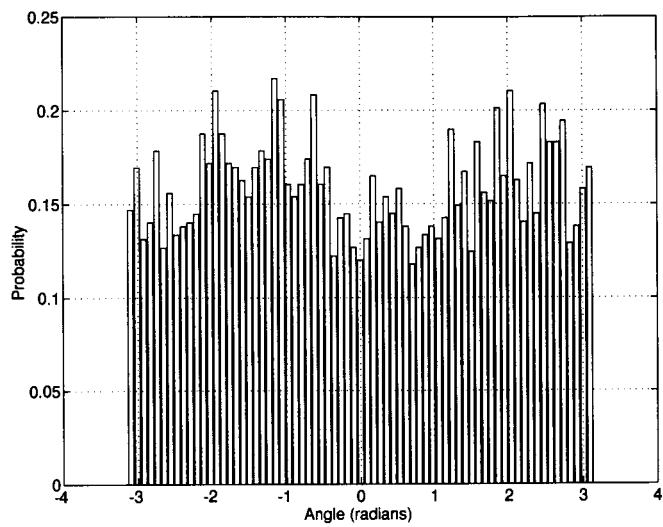
Figure 4.2: Simulated Phase Distribution

## 4.3.2 Other Channel Statistics



* Top curve – theoretical, Bottom curve – measured.
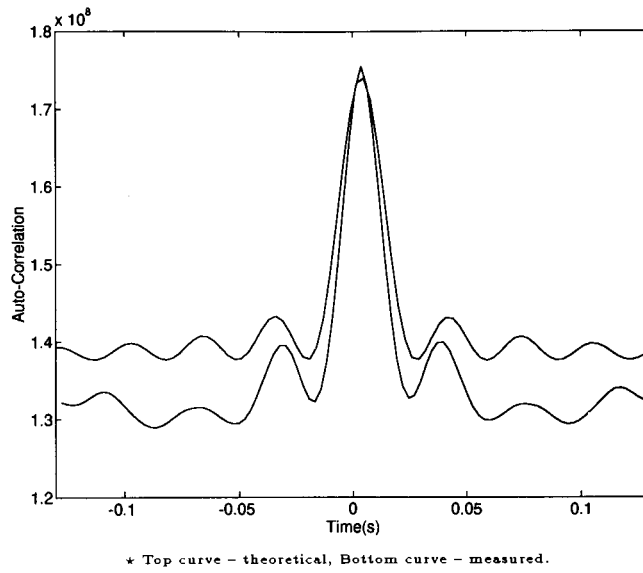
Figure 4.3: Simulated Envelope Auto-correlation



* Envelope curve – theoretical, High frequency curve – measured.
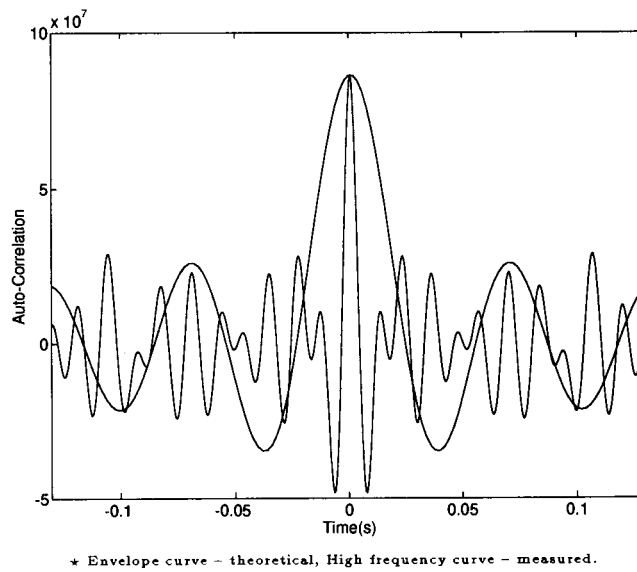
Figure 4.4: Simulated Signal ($I$) Auto-correlation

35

The auto-correlation at a given instant in time, $t_o$, was generated using a 10 sec block of data. 5 sec of data on either side of $t_o$ was used to compute the auto-correlation, but only 0.13 sec on either side of $t_o$ is shown in the plots. Both figures show the measured results along with the theoretical curve. In each case the measured results agrees closely with theory.

In Figure 4.4, the $I$ signal auto-correlation, there are sub-peaks seen in the measured auto-correlation which are not seen in the theoretical auto-correlation function. These peaks are due to the periodic nature of the modulation on $I$. The theoretical plot assumes no modulation, simply pure carrier. The measured signal auto-correlation closely matches the theoretical autocorrelation which suggests that the RAND function supplied with the 'C' compiler was adequate for this purpose.

## 4.3.3   Time Domain and Frequency Domain Plots
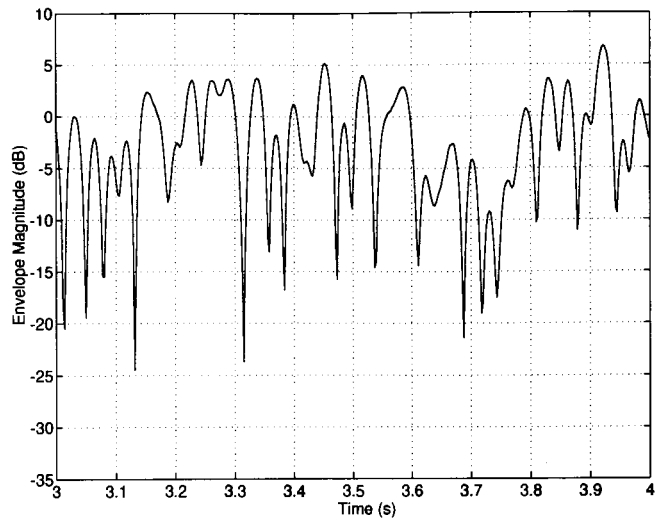


Figure 4.5: Simulated Fading Envelope
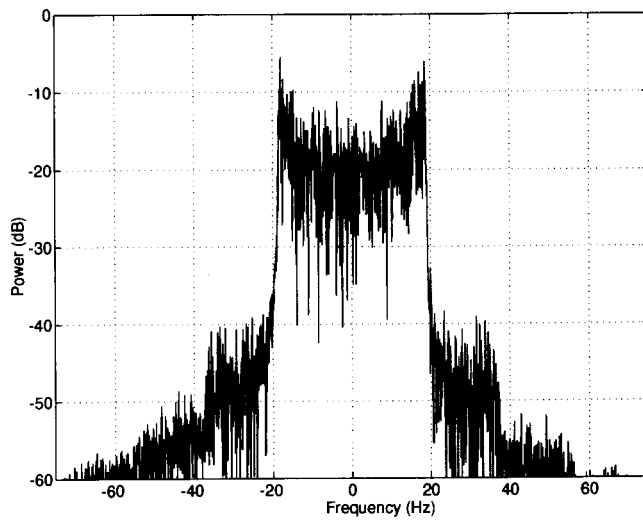


Figure 4.6: Simulated Fading Spectrum

Figure 4.5 shows the fading envelope for channel 1 of the simulator for a period of 1s.

The fading spectrum was generated using a 10 sec block of data. The results indicated that the doppler frequency was 20Hz which corresponds to a vehicle traveling at 26.5km/hr.

## 4.4    Spatial Channel Simulator Performance
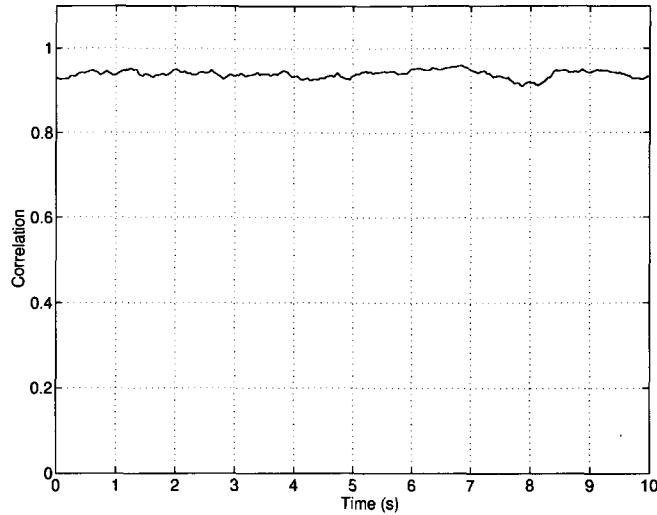


Figure 4.7: Simulated Envelope Cross Correlation Coefficient ($\rho_{12}$)

The correlation coefficient at a given instant in time, $t_o$, was generated using a 1 sec block of data. $\frac{1}{2}$sec of data on either side of $t_o$ was used to compute the correlation coefficient at time $t_o$.

The simulator was programmed for an $I$ and $Q$ cross-correlation matrix given in Figure 3.3. Comparing this matrix to Figures 4.9 and 4.10 shows that the simulator accurately reproduced the correlation between antenna channels. Figure 4.8 shows the correlation between the envelopes of the 2 antenna channels. The programmed matrix was to come from the field test results discussed in Section 6.2. If you compare this matrix to those in Section 6.2, you will find that they do not match. The reason for this was, the cross-correlation matrix obtained from the field tests varied greatly in time for reasons discussed in that section. As a result, a cross-correlation matrix at an arbitrary instant in time, and one which agrees with theory, was extracted from the field test measurements and used here as the desired cross-correlation matrix for the simulator. The important result is the measured cross-correlation is exactly what it was programmed to be, and it doesn't vary in time.

$$\begin{bmatrix} 1.0000 & 0.9140 & 0.8974 & 0.8620 & 0.8341 & 0.8149 & 0.7377 \\ 0.9140 & 1.0000 & 0.8899 & 0.8187 & 0.8339 & 0.6524 & 0.6351 \\ 0.8974 & 0.8899 & 1.0000 & 0.8661 & 0.8545 & 0.8592 & 0.6754 \\ 0.8620 & 0.8187 & 0.8661 & 1.0000 & 0.9218 & 0.8915 & 0.8088 \\ 0.8341 & 0.8339 & 0.8545 & 0.9218 & 1.0000 & 0.9029 & 0.7798 \\ 0.8149 & 0.6524 & 0.8592 & 0.8915 & 0.9029 & 1.0000 & 0.8804 \\ 0.7377 & 0.6351 & 0.6754 & 0.8088 & 0.7798 & 0.8804 & 1.0000 \end{bmatrix}$$

Figure 4.8: Envelope Correlation

$$\begin{bmatrix} 1.0000 & 0.9335 & 0.9420 & 0.9199 & 0.9081 & 0.8935 & 0.8540 \\ 0.9335 & 1.0000 & 0.9483 & 0.9260 & 0.9034 & 0.8600 & 0.7781 \\ 0.9420 & 0.9483 & 1.0000 & 0.8958 & 0.9097 & 0.9278 & 0.8474 \\ 0.9199 & 0.9260 & 0.8958 & 1.0000 & 0.9631 & 0.9404 & 0.9019 \\ 0.9081 & 0.9034 & 0.9097 & 0.9631 & 1.0000 & 0.9526 & 0.8917 \\ 0.8935 & 0.8600 & 0.9278 & 0.9404 & 0.9526 & 1.0000 & 0.9386 \\ 0.8540 & 0.7781 & 0.8474 & 0.9019 & 0.8917 & 0.9386 & 1.0000 \end{bmatrix}$$

Figure 4.9: I Correlation

$$\begin{bmatrix} 1.0000 & 0.9377 & 0.9473 & 0.9203 & 0.9101 & 0.8970 & 0.8518 \\ 0.9377 & 1.0000 & 0.9521 & 0.9276 & 0.9099 & 0.8578 & 0.7824 \\ 0.9473 & 0.9521 & 1.0000 & 0.8933 & 0.9015 & 0.9272 & 0.8530 \\ 0.9203 & 0.9276 & 0.8933 & 1.0000 & 0.9636 & 0.9370 & 0.9044 \\ 0.9101 & 0.9099 & 0.9015 & 0.9636 & 1.0000 & 0.9495 & 0.8777 \\ 0.8970 & 0.8578 & 0.9272 & 0.9370 & 0.9495 & 1.0000 & 0.9346 \\ 0.8518 & 0.7824 & 0.8530 & 0.9044 & 0.8777 & 0.9346 & 1.0000 \end{bmatrix}$$

Figure 4.10: Q Correlation

Figure 4.7 was included to show that the cross-correlation does not change with time. The theoretical analysis discussed in Section 3.2 suggests that this should be the case. However, for reasons discussed in Section 6.2, the cross-correlation matrix observed in the field tests did vary in time. Again, the important result was the simulator's measured cross-correlation was exactly as expected, and as it was programmed, does not change with time.

# Chapter 5

# phased array antenna

## 5.1   Synopsis of Chapter

This chapter discusses the mobile base-station, phased array antenna system that was designed and the test setup used to evaluate its performance. All the necessary transmitter, receiver and digitization hardware are discussed. The theoretical and measured performance of the antenna array are examined in a static environment. Also, the field test setup and a description of the tests performed are explained.

## 5.2   Hardware Requirements

### 5.2.1   Mobile Transmitter

The mobile transmitter was a base-band to RF direct conversion, QPSK modulator which operated at 815MHz. Figure 5.1 shows the block diagram for the transmitter.

The base-band signal was generated with a computer equipped with a TMSC25 DSP board. $I$ and $Q$ samples were written to a 2 channel DAC at a rate of 20k samples/sec. The 2 channel DAC was a part

of the 14 channel DAC described in Section 3.4. The 2 outputs of the DAC were filtered using an active LC filter, Krohn-Hite 3342R, and applied to the $I$ and $Q$ inputs of the quadrature modulator. The on channel RF signal was generated using direct upconversion. Because an HP8657A was used as the LO for the quad-mod, the transmitter had excellent hum and noise characteristics and good frequency stability.

The single step upconversion process eliminated the need for RF filtering of the signal. The output of the quad-mod was applied to a 3W Mini-Circuits power amp (ZHL-1000-3W), but the signal level was backed off to 1.5W to keep intermods low.

The DC bias and AC level on the $I$ and $Q$ signals was accurately tuned using the DSP for the same reasons discussed in Section 3.6. The DC bias was adjusted until the carrier on a modulated signal was attenuated by at least 40 dBc.

**Mobile Transmitter Specifications**

The transmitter was tested for the following specifications. The results of the testing is summarized in Table 5.1. The transmitter was operated at a fixed output level which was 3dB below the 1dB compression point of the transmitter string. For this reason, the 1dB compression point of the transmitter is not specified as a measured specification. Also, the $3^{rd}$ order intermod point is not specified. Instead, the level of the $3^{rd}$ order intermods at the fixed operating point is quoted.

1. Carrier Suppression/Feedthrough

2. $3^{rd}$ Order Intermod Levels

3. Quadrature Phase Error

4. $I, Q$ Gain Imbalance

**Carrier Suppression/Feedthrough:** Carrier Suppression was measured using the HP8495E spectrum analyzer. A dc signal was applied to $I$ and $Q$ and the RF carrier power measured ($L_1$). Next, the

Table 5.1: Transmitter Specifications

| Description | Specification |
|---|---|
| Operating Frequency | 815 MHz |
| Output Power | 1.5 W |
| Modulation | differential QPSK |
| Carrier Suppression/Feedthrough | 45 dB |
| $3^{rd}$ Order Intermods | -40 dBc |
| $I, Q$ Cross-Talk | -30 dB |
| Quadrature Phase Error | 0.9 deg. |
| $I, Q$ Gain Imbalance | 0.2 dB |

carrier was modulated with a complex, 4kHz tone and the carrier power measured again ($L_2$). Carrier suppression/feedthrough was calculated as $L_2 - L_1$ (where $L_2$ and $L_1$ are measured in dB).

**$3^{rd}$ Order Intermod Levels:** $3^{rd}$ order intermod levels were measured using the HP8495E spectrum analyzer. The carrier was modulated with a complex, 4kHz tone and the power in the $3^{rd}$ order intermods was measured relative to the power in the desired signal.

**$I, Q$ Cross-Talk:** The $I, Q$ cross-talk specification characterizes the performance of both the transmitter and the receiver working together. $I, Q$ cross-talk can be introduced in both the transmit modulator and the receive demodulator, but lack of equipment prevented the transmitter and the receiver from being tested separately. See Section 5.2.2 for an explanation of the $I, Q$ cross-talk measurements.

**Quadrature Phase Error:** Quadrature phase error was measured using the HP8753D network analyzer. Port 1 of the analyzer was connected to the LO input of the modulator IC and port 2 was connected to the quadrature LO output of the modulator IC. The quadrature phase error was then measured directly using the network analyzer.

$I, Q$ **Gain Imbalance:** $I, Q$ gain imbalance was measured using the HP8921's ac signal level capability. A complex, 4kHz tone was generated on the $I$ and $Q$ outputs of the DSP and the HP8921 used to measure the signal level of $I$ and $Q$.

**Note:** Other specifications such as frequency stability, hum and noise, phase noise, etc. were all very good because HP8657A signal generators were used as the LOs in the transmitter.
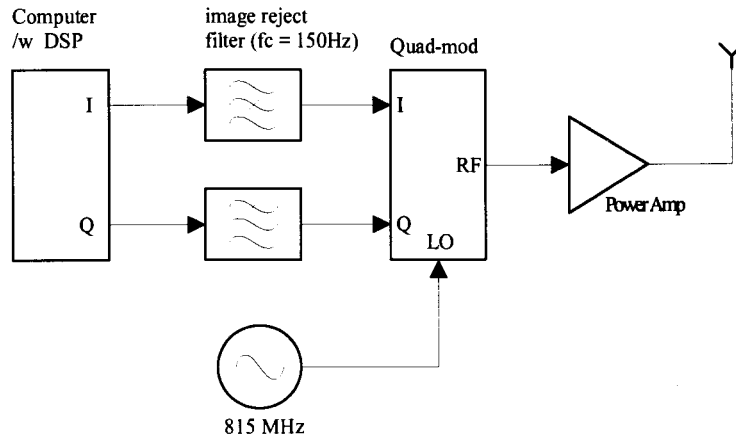


Figure 5.1: Transmitter Block Diagram

## 5.2.2 Base-Station Receiver

**Receiver Hardware**

The receiver actually consisted of seven independent, but identical, receiver channels. The following is a description of one of the seven receiver channels.

The receiver is a three step down-conversion type, with the first IF at 45 MHz and the second IF at 455 kHz. The receiver string starts with a broadband RF filter and then LNA which provides gain and establishes the noise figure of the receiver. The LNA output is passed through a ceramic band pass filter and then to the first mixer. The local oscillator for this mixer is an HP8657A signal generator operating 45 MHz above the receive frequency of 815 MHz.

The mixer output passes through a crystal filter, with a center frequency of 45 MHz, to the second mixer stage IC. This IC houses both the second mixer and most of the receiver gain. The second LO operates at 455 kHz below the 45 MHz IF frequency and is also generated by a HP8657A signal generator.

At the IF frequency of 455 kHz, the signal enters the QPSK demodulator IC. A Marconi 2022 signal generator was used to generate twice the IF frequency of 455 KHz because the demodulator employs a digital divider type $90^o$ phase shifter. The two outputs of the quadrature demodulator, $I$ and $Q$, are buffered and filtered to remove the second image. The two outputs are then made available to the outside world.

Seven of the receiver channels described above were packaged together to create the 7 channel receiver needed to complete the field tests. Each of the 7 elements of the antenna were connected to a separate receiver. Careful attention was made to ensure all cable lengths and gains were consistent between channels before the tests were done.

A block diagram of the receiver can be seen in Figure 5.2 and the receiver schematic can be seen in Figure 5.3. The block diagram of the receiver (Figure 5.2) also shows the design specifications of noise figure, sensitivity, gain, input 1dB compression point and input $3^{rd}$ order intercept point. The design

46

specifications seen in Figure 5.2 very closely match the measured performance specifications seen in Table 5.2. The exception was the sensitivity of the receiver. The designed receiver sensitivity was -104 dBm, but the measured sensitivity was only -94 dBm. The difference was due to small miss-matches throughout the receiver chain, but primarily at the IF crystal filter.

**Base-Station Receiver Specifications**

All 7 receive channels were tested for the following performance specifications. The specifications quoted in Table 5.2 represent the worst case of all 7 channels tested. Whenever baseband measurements were performed using the HP8921, special baseband filters (ie. C-message or de-emphasis filtering) inside the HP8921 were not used to improve the measurements. The baseband filters on the HP8921 were set to <20Hz HP and 20kHz LP to model the inputs of the digital recorder.

1. Bandwidth

2. Sensitivity

3. 1 dB Compression Point

4. Dynamic Range

5. Minimum and Maximum $I$, $Q$ AC Signal Level

6. $I, Q$ Cross-Talk

7. Quadrature Phase Error

8. $I, Q$ Gain Imbalance

9. Spurious Response

**Sensitivity:** Sensitivity was measured using the SINAD capabilities of the HP8921. A carrier modulated with a complex, 4kHz tone was injected into the front end of the receiver and the HP8921 used to measure

Table 5.2: Receiver Specifications

| Description | Specification |
|---|---|
| Operating Frequency | 815 MHz |
| Bandwidth | 10 kHz |
| Sensitivity | -94 dBm |
| Input 1 dB Compression Point | -44 dBm |
| Dynamic Range | 50 dB |
| Input $3^{rd}$ Order Intercept | -37 dBm |
| Minimum / Maximum $I, Q$ AC Signal Level | -40 dBV / +10 dBV |
| $I, Q$ Cross-Talk | -30 dB |
| $I, Q$ Gain Imbalance | 1 dB |
| Spurious Response | > 50 dB |

the baseband SINAD on $I$ and $Q$. No special baseband filtering was used to improve the sensitivity measurement (ie. no C-message or de-emphasis filtering). The baseband filters on the HP8921 were set to <20Hz HP and 20kHz LP to model the inputs of the digital recorder. The signal strength of the injected RF was lowered until the measured SINAD fell to 12dB. The resulting RF signal level was recorded as the sensitivity of the receive channel under test.

**1 dB Compression Point:** The 1 dB compression point was measured using the HP8921's ac signal level capabilities. A carrier modulated with a complex, 4kHz tone was injected into the front end of the receiver. The injected RF level was initially set to the 12dB SINAD sensitivity of the receiver then increased in 1dB steps until the receiver began to compress. At each step, the input RF level and baseband ac signal level were recorded. The 1dB compression point was determined using graphical techniques and is with reference to the input RF power level.

**Dynamic Range:** The dynamic range is simply defined as (1dB compression point) - (sensitivity).

**Input $3^{rd}$ Order Intercept:** The input $3^{rd}$ order intercept point was measured using the HP dynamic signal analyzer. Two tones, one at 815MHz + 2khz and one at 815MHz + 3kHz were injected into the front end of the receiver. Both signals were at the same power level and had a combined power 6dB below the compression point of the receiver. The baseband $3^{rd}$ order intercept power (power at 1kHz) was then measured using the HP dynamic signal analyzer and compared to the baseband power at 2kHz and 3kHz. From the measured results, and the generalization that for every 1dB increase in input power the $3^{rd}$ order intercept power increases by 3dB, the input $3^{rd}$ order intercept point was calculated.

**Minimum / Maximum $I, Q$ AC Signal Level:** The minimum and maximum $I, Q$ ac signal levels were measured using the HP8921. They represent the base-band ac level in dBV at the 12dB SINAD sensitivity point and at the 1dB compression point respectively. These two levels fall within the dynamic range of the digital recorder. Note: The dynamic range of the digital recorder was 96dB (-84dBV — +12dBV).

**$I, Q$ Cross-Talk:** $I, Q$ cross-talk was measured using the HP8921. This specification characterizes the performance of both the transmitter and the receiver working together. $I, Q$ cross-talk can be introduced in both the transmit modulator and the receive demodulator, but lack of equipment prevented the transmitter and the receiver from being tested separately. A carrier modulated with a complex, 4kHz tone was injected into the front end of the receiver and the HP8921 used to measure the ac signal level of the receiver $I$ output. The $I$ modulation was then removed from the transmitter and the ac signal level of the receiver $I$ output was measured a second time. The difference between these two readings was recorded as the $I, Q$ cross-talk. Proper measurement of $I, Q$ cross-talk requires a coherent receiver. This was accomplished by phase locking the transmit and receive LOs and using a delay line on the first LO of the receiver to null out any phase difference between the transmitter and the receiver.

**$I, Q$ Gain Imbalance:** $I, Q$ gain imbalance was measured using the HP8921's ac signal level capability. A carrier modulated with a complex, 4kHz tone was injected into the front end of the receiver and the HP8921 used to measure the base-band signal level of $I$ and $Q$.

**Spurious Response:** The receivers spurious response was measured using the signal generator in the HP8921 and a second, external HP8657A signal generator. The output of the two signal generators were summed using a power combiner and the resulting signal fed into the front end of the receiver under test. The HP8921 was used as the carrier while the HP8657A was used the interferer. The signal level of the carrier was set to $L_c$, 3dB above the sensitivity limit of the receiver. The SINAD of the receiver base-band signal was measured using the HP8921. At certain interferer frequencies $f_i(i = 1, 2, 3 \ldots, N)$ the receiver had a response which showed up as a reduction in the base-band SINAD of the receiver. At the given frequencies, $f_i$, the power of the interferer was increased to a level, $L_i$, such that the SINAD fell back to 12dB. The spurious response at $f_i$ was given by $SR_i = L_i - L_c(i = 1, 2, 3 \ldots, N)$. For all $i$, it was found that $SR_i > 50dB$ as quoted in Table 5.2.

**Note:** Other specifications such as frequency stability, hum and noise, phase noise, etc. were all very good because HP8657A signal generators were used as the LOs in the receiver.

### Receiver Calibration

For the gathered data to mean anything, any distortions due to the receiver had to be removed. The magnitude response and phase response of each receiver was measure across the 10kHz bandwidth of the receiver. The measured responses permitted each receiver to be individually characterized. It was determined that the best procedure for characterizing the receivers was to use the 1 min of stationary data recorded at the beginning of the 8 tone test. Calibration in the lab was considered, but field calibration permitted calibration of the antenna elements, antenna feed and receivers without the use of an anechoic chamber and conducted laboratory calibration would ignore any effects due to the antenna elements and antenna feed.

Stationary data recorded during the 8 tone test (see Section 5.4.2) was used to calibrate the receiver. At each of the 8 tones, the phase and magnitude of each receiver channel was analyzed. The phase and magnitude of each receiver channel was then calculated using linear interpolation between the 8 measured values. This data was used to remove any distortion introduced by the receiver.

| Stage: | Front End Filter | LNA | RF Filter | 1st IF Mixer | 1st IF Filter | IF Amp. | 2nd IF Mixer | 2nd IF Filter | IF Amp. | IQ Demodulator | Image Reject Filters |
|---|---|---|---|---|---|---|---|---|---|---|---|
| Power Gain (dB) | -3 | 8 | -3 | 12 | -3 | 16 | 3 | -3 | 57 | 12 | 0 |
| Cumlative Gain (dB) | -3 | 5 | 2 | 14 | 11 | 16 | 19 | 16 | 73 | 85 | 85 |
| Cumlative Gain (linear) | 0.501 | 3.162 | 1.585 | 25.119 | 12.589 | | | | | 85 | 85 |
| Noise Figure (dB) | 3 | 4 | -3 | 8 | 3 | | | | | | |
| Noise Factor | 1.995 | 2.512 | 0.501 | 6.310 | 1.995 | | | | | | |
| Cumlative Noise Factor | 1.995 | 5.012 | 4.854 | 8.204 | 8.244 | | | | | | |
| Cumlative Noise Figure | 3.00 | 7.00 | 6.86 | 9.14 | 9.16 | | | | | | |
| | | | | | <-- Units in dBm | Units in dBV --> | | | | | |
| Input P$_1$ | 999.00 | -21.00 | 999.00 | -14.00 | 999.00 | -30.00 | -3.00 | 999.00 | -1.50 | -12.00 | 14.00 |
| Input P$_1$ Ref. to Front End | 999.00 | -18.00 | 994.00 | -16.00 | 985.00 | -22.70 | -18.41 | 371.20 | -17.83 | -44.15 | -38.69 |
| Input IP$_3$ Point | 999.00 | -7.00 | 999.00 | 0.00 | 999.00 | -17.00 | 10.00 | 999.00 | 14.00 | 8.00 | 29.00 |
| Input IP$_3$ Ref. to Front End | 999.00 | -4.00 | 994.00 | -2.00 | 985.00 | -17.63 | -13.34 | 371.20 | -11.78 | -36.35 | -32.84 |



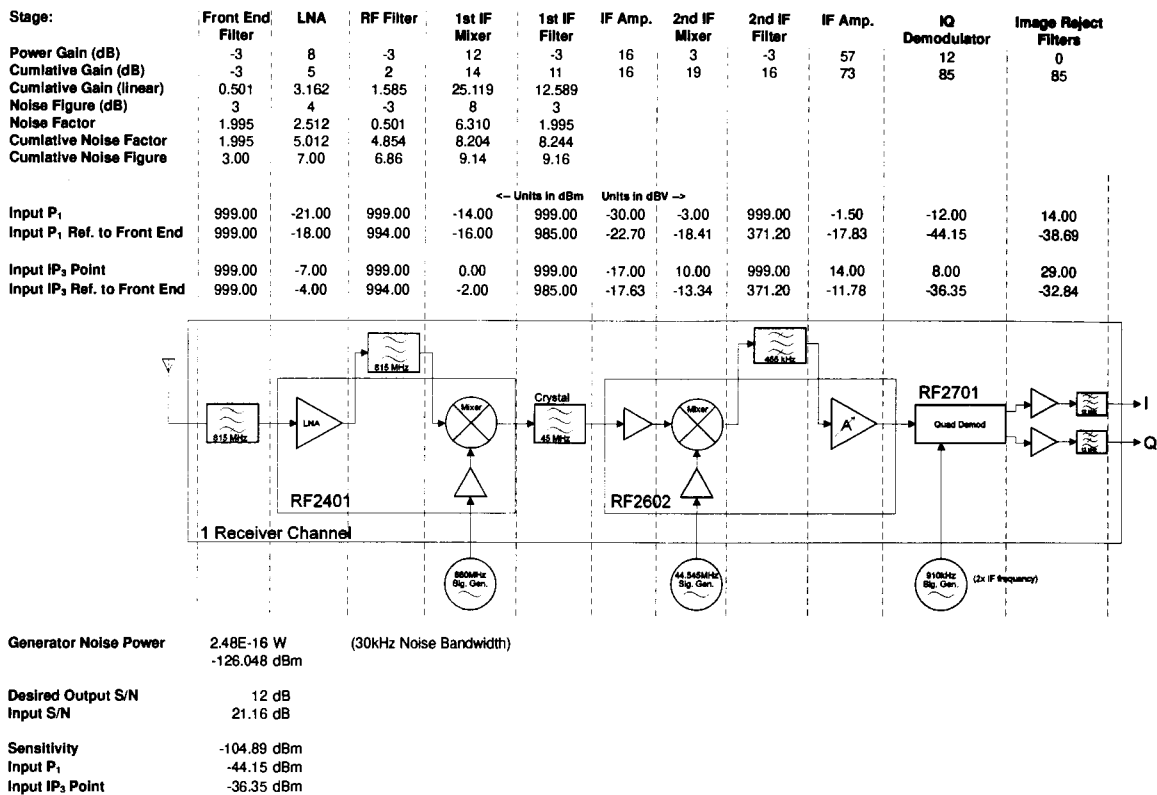| | | |
|---|---|---|
| Generator Noise Power | 2.48E-16 W | (30kHz Noise Bandwidth) |
| | -126.048 dBm | |
| Desired Output S/N | 12 dB | |
| Input S/N | 21.16 dB | |
| Sensitivity | -104.89 dBm | |
| Input P$_1$ | -44.15 dBm | |
| Input IP$_3$ Point | -36.35 dBm | |

Figure 5.2: Base-station Receiver Block Diagram

In the case of the single tone test, the receiver was calibrated using the stationary data recorded at the beginning of the single tone test not the 8 tone test. This was because the single tone tests were very narrow band and the receiver only had to be calibrated at the one frequency.
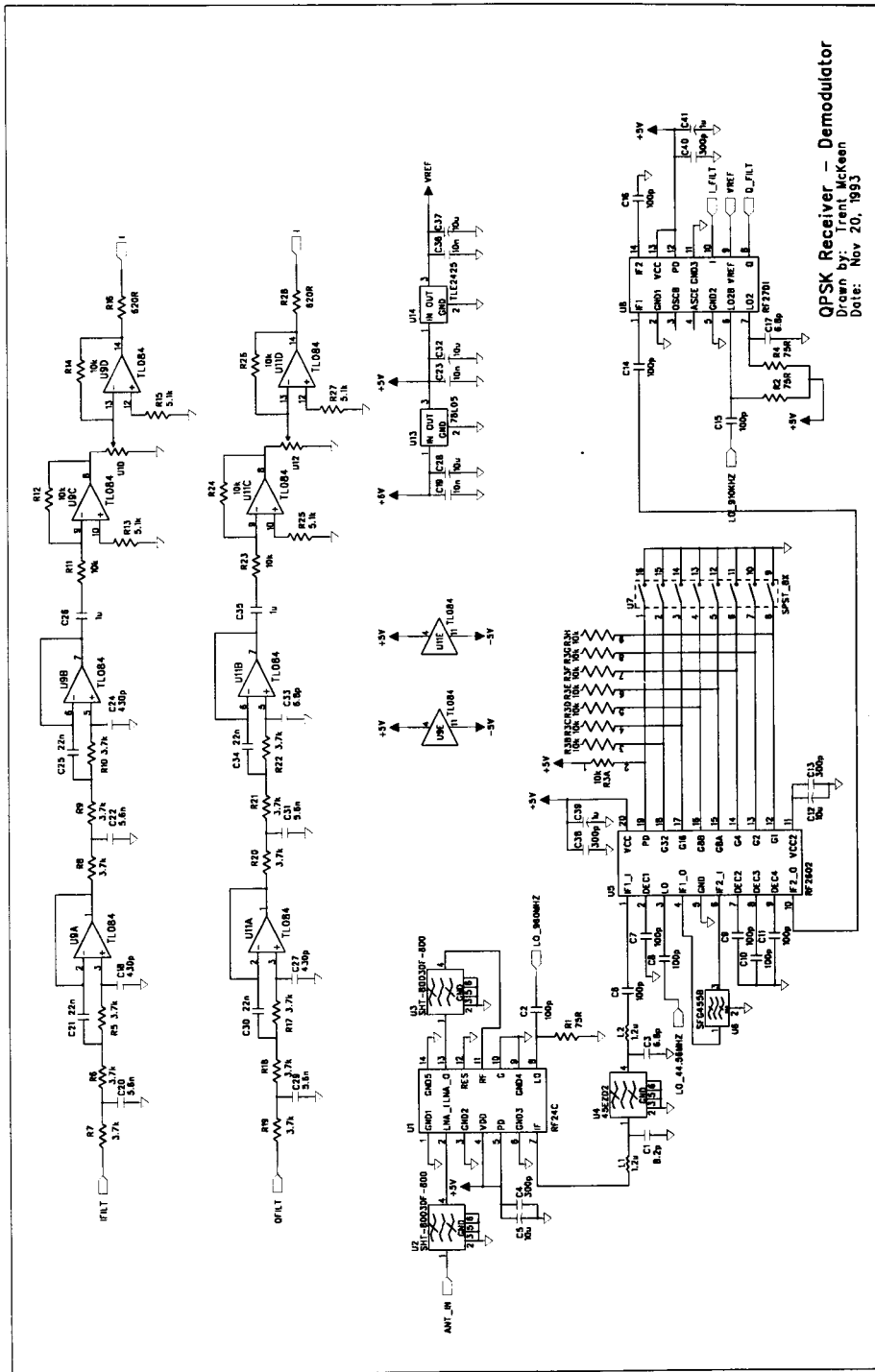
Figure 5.3: QPSK Receiver/Demodulator – One channel

## 5.2.3 Antenna

An array of identical elements all of identical magnitude and each with a progressive phase is referred to as a uniform array. The antenna array examined in this paper was a uniform array. Figure 5.4 shows the geometry of the array. The array factor can be obtained by considering the elements to be point sources. If the actual elements are not isotropic sources, the total field can be formed by multiplying the array factor of the isotopic sources by the field of a single element.
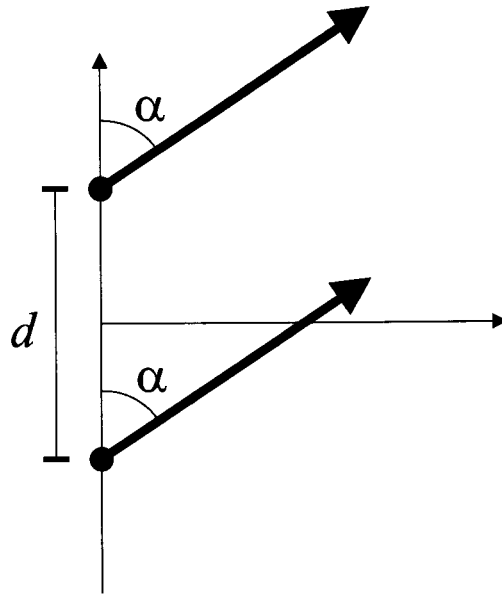
Figure 5.4: Geometry of a Two Element Linear Array

The array factor is given by

$$S = \sum_{n=1}^{N} e^{j(n-1)(kd\cos\alpha+\beta)} \tag{5.1}$$

53

$$
\begin{array}{lll}
N & = & \text{the number of elements in the array} \\[4pt]
\alpha & = & \text{arrival angle of the incoming signal} \\[4pt]
\text{where} \quad \beta & = & \text{incremental phase difference between elements} \\[4pt]
d & = & \frac{\lambda}{2} \\[4pt]
k & = & \frac{2\pi}{\lambda}
\end{array}
$$

Which can be simplified to the following expression.

$$
AF = \frac{1}{N} \left[ \frac{\sin\left(\frac{N}{2}\psi\right)}{\sin\left(\frac{1}{2}\psi\right)} \right]
\tag{5.2}
$$

where $\quad \psi \quad = \quad kd\cos\alpha + \beta$

The base-station antenna discussed in this paper was a 7 element, phased array antenna. Each of the 7 individual elements which made up the phased array antenna were omni-directional patch antennas which were positioned on a wooden support and spaced $\frac{\lambda}{2}$ apart. Figure 5.5 shows the radiation pattern for one of the patch antenna elements.

Because the individual elements of the array were omni-directional, the radiation pattern for the array was simply the array factor given in Equation 5.2 with $N = 7$.

The theoretical radiation pattern for a seven element array is shown in Figure 5.6. This figure shows the antenna array functioning as a broadside array (ie $\alpha = \frac{\pi}{2}, \beta = 0$).

By controlling the phase excitation between elements, it is possible to direct the major radiation beam in an arbitrary direction. If the maximum radiation from the array is to be oriented at an angle $\theta_o$, then the phase excitation $\beta$ between the elements must be adjusted so that

$$
\psi = kd\cos\alpha + \beta = kd\cos\theta_o + \beta = 0
\tag{5.3}
$$

Therefore,

$$
\beta = -kd\cos\theta_o
\tag{5.4}
$$

Figure 5.7 shows the radiation intensity the 7-element phased array antenna would see if the radiator was placed at boresight ($\alpha = \frac{\pi}{2}$) and the relative phase excitation between elements ($\beta$) is adjusted. The
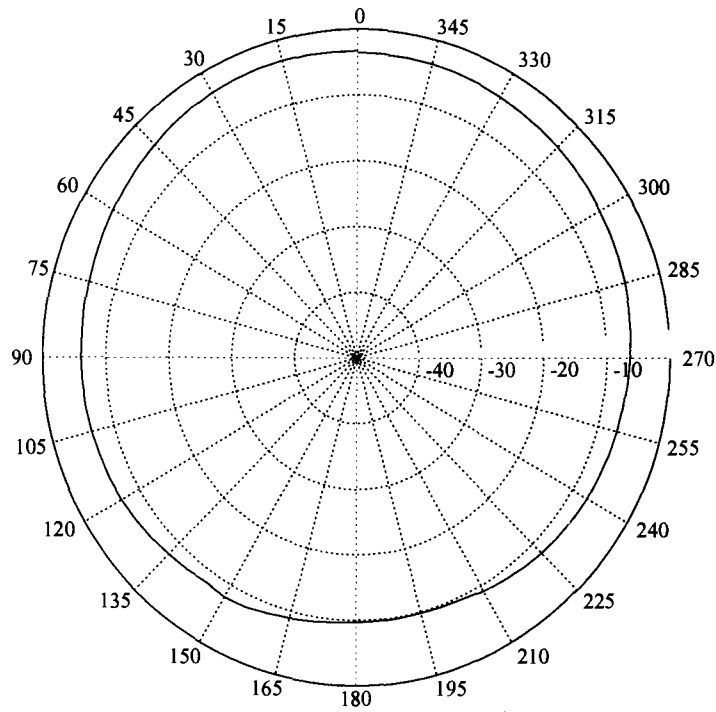
Figure 5.5: Radiation Pattern for Single Element of the Antenna Array

purpose of this pattern is to show that the antenna can indeed track the vehicle as it moves through the environment. A simple tracking algorithm would scan a full 360°s and conclude the vehicle was at the position of maximum power. If this same function was plotted versus $\theta_o = \cos^{-1}\left(-\frac{\beta}{kd}\right)$ instead of $\beta$, one would obtain the antenna pattern shown in Figure 5.6. This can be seen by substituting Equation 5.4 into Equation 5.2 and setting $\alpha = 0$.
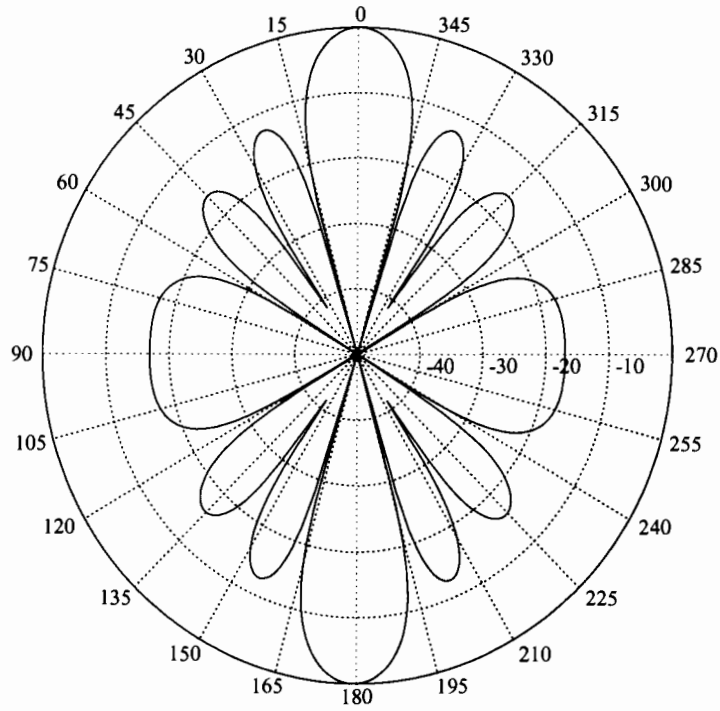
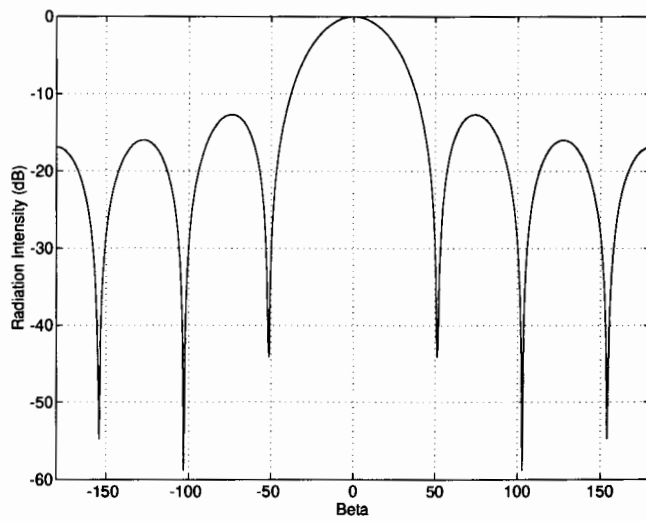Figure 5.6: Radiation Pattern for the 7 Element Antenna Array



Figure 5.7: Theoretical Steering Pattern for a 7 Element Linear Array

56

## 5.2.4  Data Digitization and Storage

During the field tests, the fourteen baseband signals were recorded on Alesis ADAT, 16 track recorder permitting the received signals to be played back at any time. This process is depicted in Figure 5.8(a).

The complexity of the analysis performed on the received signals prevented the analysis from being done in real time. As a result, the received signals had to be digitized and stored for analysis at a later date. The sheer quantity of data made this a difficult task.

A PC equipped with a TMSC25 DSP board was used to digitize and store the received signals on a SCSI disk drive. When the disk drive was full, the data was written to a CD and the SCSI drive erased permitting new data to be digitized. The received signals, having frequency components up to 5kHz, was sampled at 20kHz. To sample 14 channels at 20kHz required a transfer rate to the SCSI drive which was beyond the capability of the PC. As a result, only one track of the recorder was digitized at a time. This created a problem of synchronization between the tracks as they were being digitized. The solution was to record a 5kHz tone on track 16 and phase lock a 20kHz clock to this sync tone. The 20kHz clock was then used as the sample clock in the A/D converter. There was also some circuitry to count 4096 cycles of the 5kHz sync tone before the 20kHz clock was enabled. This ensured that the PLL was locked before sampling began. It also ensured that all sampling began at the same instant in time relative to the tape. A block diagram of the digitization process in shown in Figure 5.8(b).
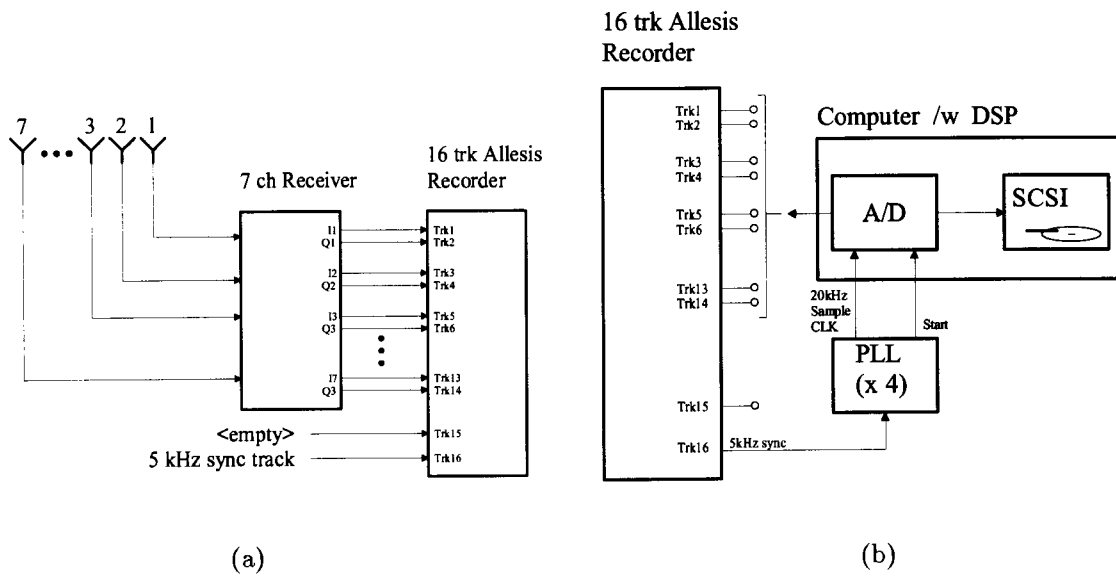
**16 trk Allesis Recorder**

7 ··· 3 2 1

7 ch Receiver

16 trk Allesis Recorder

I1
Q1
Trk1
Trk2

I2
Q2
Trk3
Trk4

I3
Q3
Trk5
Trk6

I7
Q3
Trk13
Trk14

<empty>
Trk15

5 kHz sync track
Trk16

(a)

**Computer /w DSP**

Trk1
Trk2

Trk3
Trk4

Trk5
Trk6

Trk13
Trk14

A/D

SCSI

20kHz
Sample
CLK

Start

Trk15

PLL
(x 4)

Trk16  5kHz sync

(b)

Figure 5.8: Data Sampling and Storage Block Diagram

## 5.3   The Field Test Setup

### 5.3.1   Mobile

The mobile functioned as the transmitter in the field tests. The transmitter described in Section 5.2.1 was placed in a car and a car battery with a 600 W power inverter was used to power the equipment inside the vehicle. An omni-directional whip antenna, placed on the roof of the car, functioned as the transmit radiator. During the field tests, the mobile was sent out to drive around a typical urban environment while continuously transmitting an RF signal. Figure 5.11 is a view from the base-station of the urban environment the vehicle drove through. The vehicle was restricted to the area in the upper left hand corner of the picture. Figure 5.9 and  5.10 show the vehicle and the transmitter inside the vehicle.
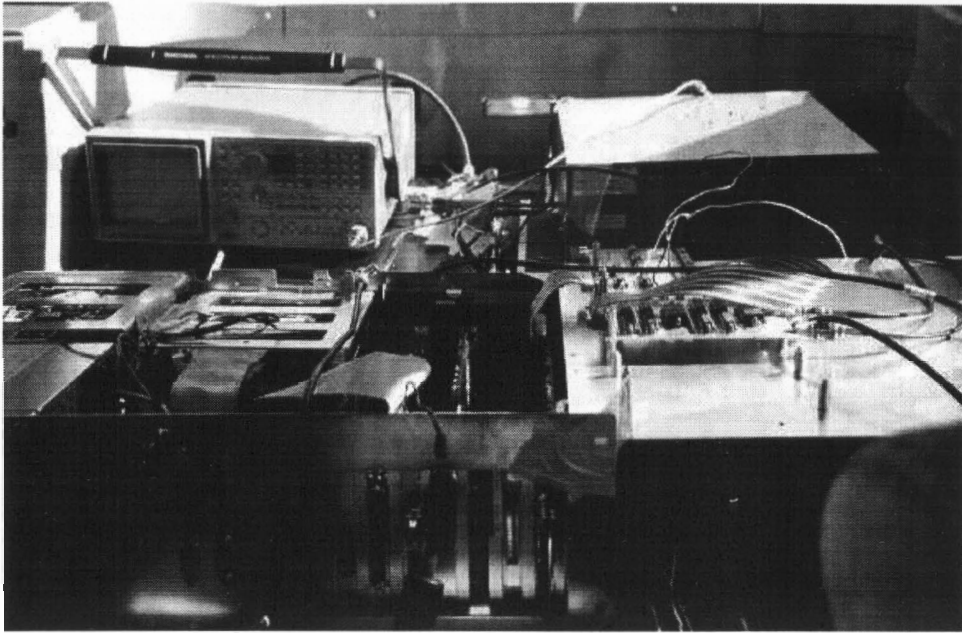


Figure 5.9: Mobile Transmitter Equipment – View 1

Figure 5.10: Mobile Transmitter Equipment – View 2



Figure 5.11: Field Test Urban Environment

## 5.3.2  Base-station

The base-station was placed on the roof of a building overlooking the route of the mobile unit. The base-station antenna consisted of the 7 element antenna described in Section 5.2.3. Each of the 7 individual antenna elements connected to one of the 7 receivers. The output of each of the 7 receivers was a complex, base-band signal, resulting in 14 base-band signals. All 14 of these signals were recorded on an Allesis ADAT, 16 channel, multi-track recorder. A 5kHz tone was also recorded on one of the 2 extra tracks on the recorder providing the capability of track synchronization during the digitization process. Photographs of the base-station setup can be seen in Figure 5.12 and 5.13.
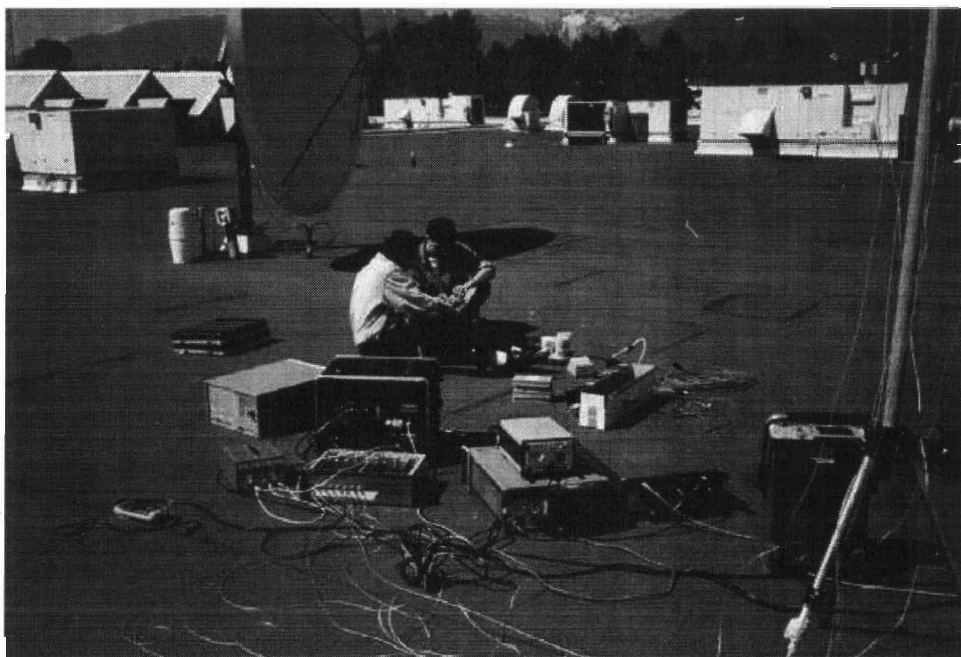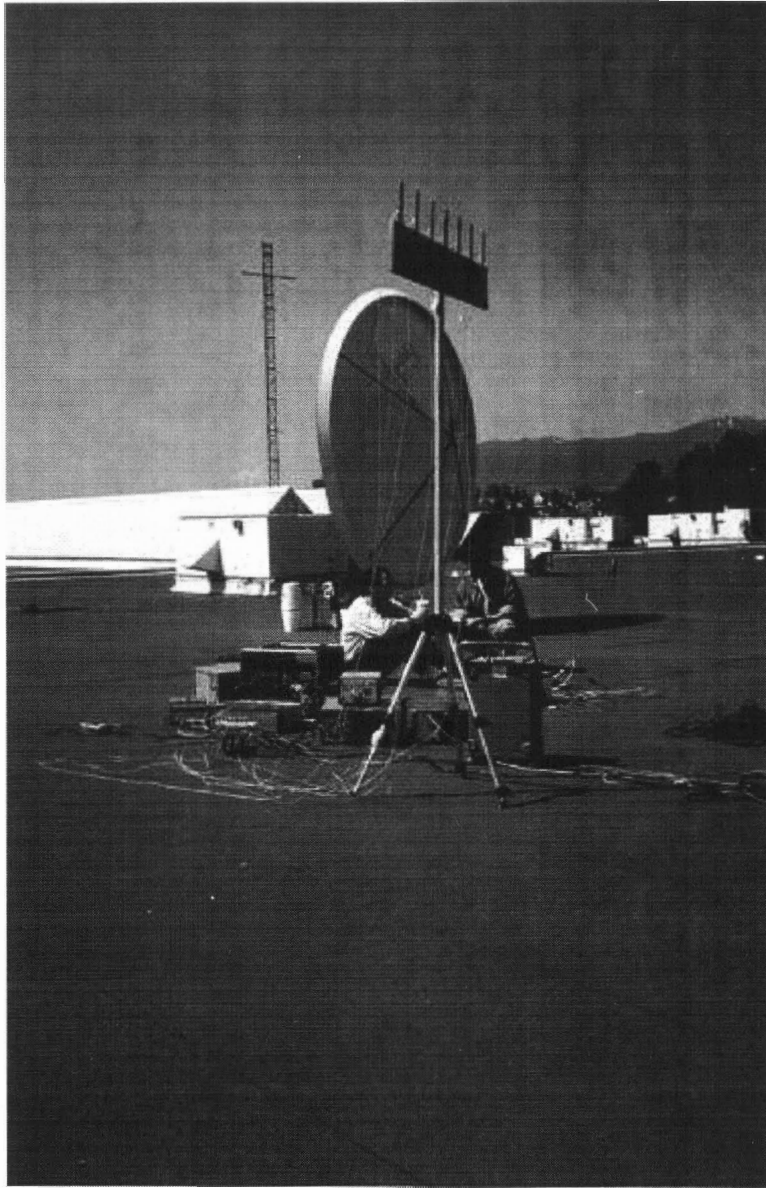


Figure 5.12: Base-station Receiver Setup – View 1

61

Figure 5.13: Base-station Receiver Setup – View 2

## 5.4 Description of Tests

The following is the step by step procedure followed to gather and digitize the field test data.

1. The vehicle driver drove to a specific "starting point" which was in visual sight from the base-station.

2. The RF transmission was initiated at the mobile unit.

3. The transmitted power was adjusted so the received signal was very strong (-10dBV). This was a line of sight transmission so the signal would drop about 30dB as soon as the vehicle entered the urban environment.

4. The tape recorder was started.

5. After 45 sec of motionless data was recorded, the vehicle proceeded into the urban environment and began to navigate the predetermined route.

6. The vehicle drove around its route and the transmitted signal was recorded for 10 minutes.

7. The recorded signals were digitized and stored on CD ROM.

The procedure above was repeated three times for three different RF transmissions. The three different signals transmitted are described below.

### 5.4.1 Single Tone

The first test consisted of transmitting a single, complex tone at 4 kHz. A complex tone is not symmetric about the carrier (or 0 after demodulation). In this case one would see a spur at $f_c + 4\text{kHz}$, but not one at $f_c - 4\text{kHz}$. This test permitted

- Correlation analysis between antenna elements

- Beam steering and vehicle tracking

- Measuring RF spectrum of fading environment

- Measuring the envelope and phase statistics of the fading environment

## 5.4.2 Eight Tone

The second test consisted of transmitting 8 complex tones equally spaced from -5 kHz to +5 kHz. This test permitted the receiver channels to be characterized over the passband of the receiver.

## 5.4.3 Data

The third test involved transmitting a known data sequence using differential QPSK modulation. This test allowed

- Effects of the fading environment on BER

- Improvements in BER due to angle diversity

- Proof of concept for a base-band directional antenna

Refer to[4] for more information on this test.

## 5.4.4 Data Plus Interferer

The fourth test involved transmitting a known data sequence using differential QPSK modulation and also positioning another white noise radiator at some angle $\theta$ relative to the receive antenna boresight. This test allowed investigation into null steering of directional antennas to reduce co-channel interference. Refer to[14] for more information on this test and null steering.

# Chapter 6

# field tests

## 6.1 Synopsis of Chapter

This section examines the behavior of a phased array base-station antenna in a real urban environment. Field tests were performed to characterize the fading environment as seen by a multi-element base-station antenna and then use those characteristics in the design of the spatial channel simulator. The field tests were to validate the mathematical model described in Section 2. If the statistical characteristics of the model agree with what was observed in the field, then the model could be used to accurately simulate the environment. The primary goal of the field tests was to obtain the cross-correlation matrix for the different antenna elements.

A number of fading characteristics were measured and are presented here. A summary of the measured characteristics is the following.

- The probability distribution of the fading signal magnitude

- The probability distribution of the fading signal angle

- The correlation coefficient between each of the different antenna elements (cross-correlation matrix)

- The fading rate

- The auto-correlation of the fading signal


## 6.2  Field Test Results

After the baseband signals were digitized, they were post-processed before they were analyzed. The post-processing consisted of compensating for the receiver, then filtering the sampled data. The filtering was done to further reduce any interfering signals such as ones at dc (produced by LO feedthrough in the quad-mod) and the negative image (due to non-linearities in the quad-mod).

In the case of the complex tone data, the samples were also downconverted further before they were filtered and then resampled after filtering. The complex tone consisted of a very narrow band signal (about 30Hz) at 4kHz. It was possible to get away with a much lower sampling rate and, as a result, less data, if the 4khz signal was down converted to 0Hz, filtered and then resampled at 1/50th the original sampling rate.

After post-processing, the baseband data was analyzed using MATLAB to obtain the following plots.

## 6.3 Single Channel Performance

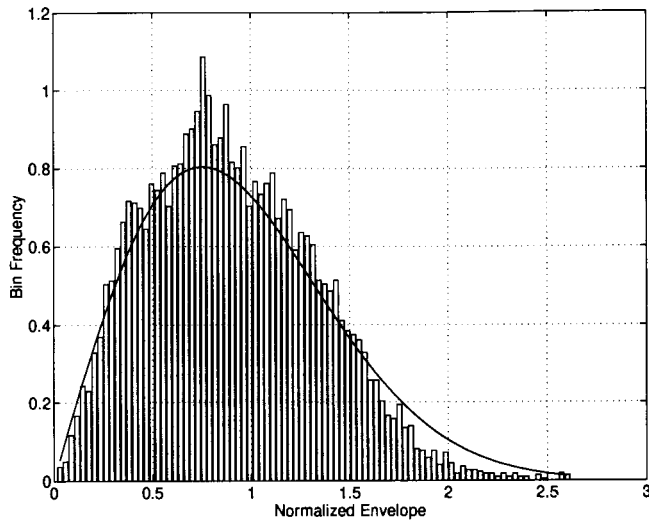### 6.3.1 Measured Probability Density Functions



Figure 6.1: Field Envelope Distribution

Figure 6.1 shows the probability distribution function for both the theoretical and measured fading signal amplitude. The solid line represents the theoretical distribution while the bars show the measured histogram. Figure 6.2 shows the cumulative distribution function for both the theoretical and measured fading signal amplitude and Figure 6.3 shows the probability distribution function for the measured fading signal phase. The probability density functions were generated using 10 sec. worth of data. Both the envelope and phase distributions have the expected behavior.
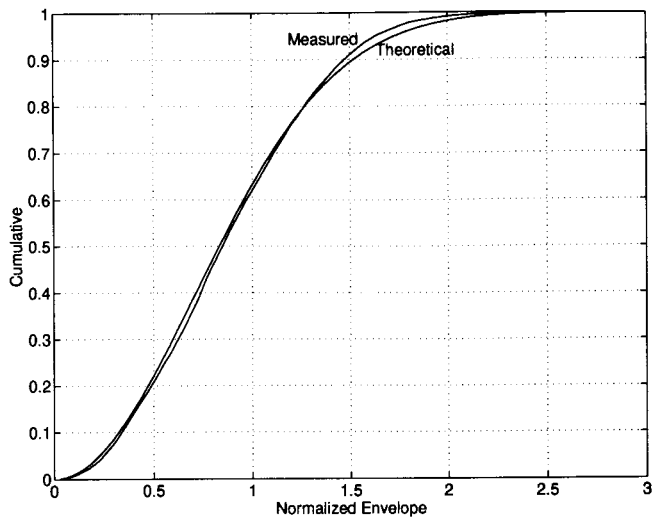
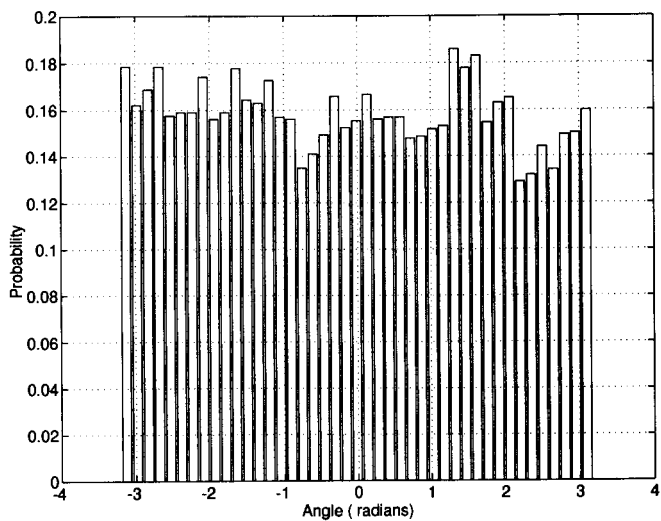Figure 6.2: Field Envelope Cumulative Distribution



Figure 6.3: Field Phase Distribution

68

## 6.3.2 Other Channel Statistics

The auto-correlation and the level crossing rate at a given instant in time, $t_o$, was generated using a 10 sec block of data. Figures 6.4 and 6.5 show a close in view of the auto-correlation function. 10 seconds was used to improve the plot by providing a longer signal. All three figures show both measured results along with the theoretical curve. In each case the measured results agrees closely with theory.

In Figure 6.4, the envelope auto-correlation, the measured auto-correlation is slightly below the theoretical one. This is due to the mean of the measured signal envelope. The overall mean of the envelope was extracted before the auto-correlation was computed. But, variations in the mean over time due to log-normal fading will effect the average level of the envelope auto-correlation.

In Figure 6.5, the $I$ signal auto-correlation, there are sub-peaks seen in the measured auto-correlation which are not seen in the theoretical auto-correlation function. These peaks are due to the periodic nature of the modulation on $I$. The theoretical plot assumes no modulation, simply pure carrier. The envelope of the peaks closely matches the theoretical auto-correlation function.
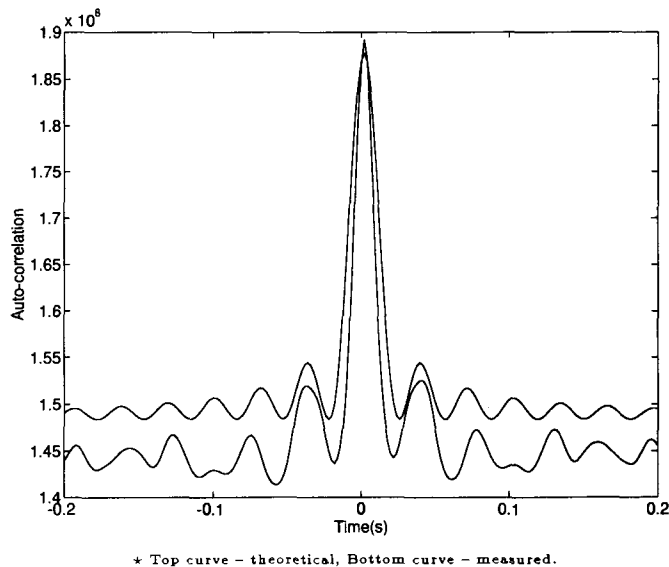


⋆ Top curve – theoretical, Bottom curve – measured.
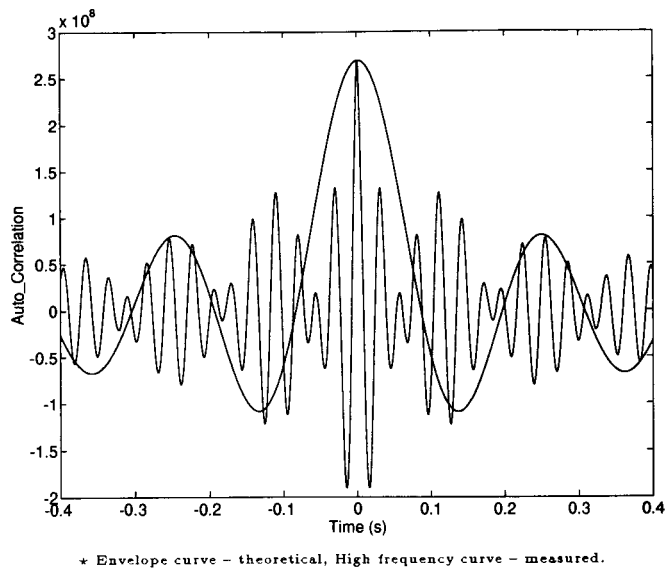
Figure 6.4: Field Envelope Auto-correlation

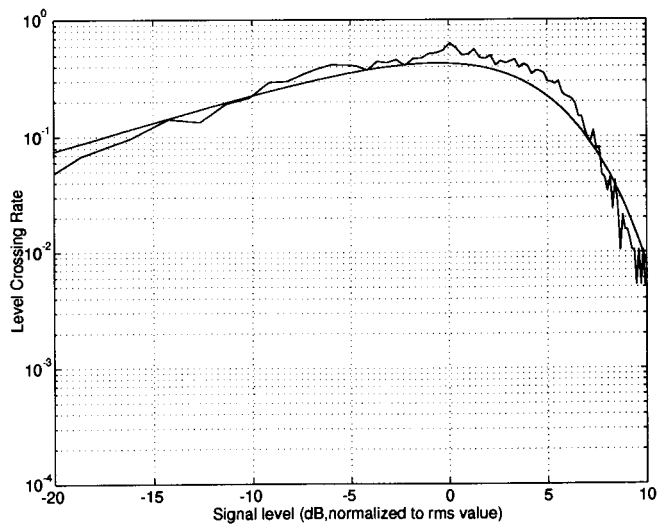Figure 6.5: Field Signal ($I$) Auto-correlation



Figure 6.6: Field Envelope Level Crossing Rate

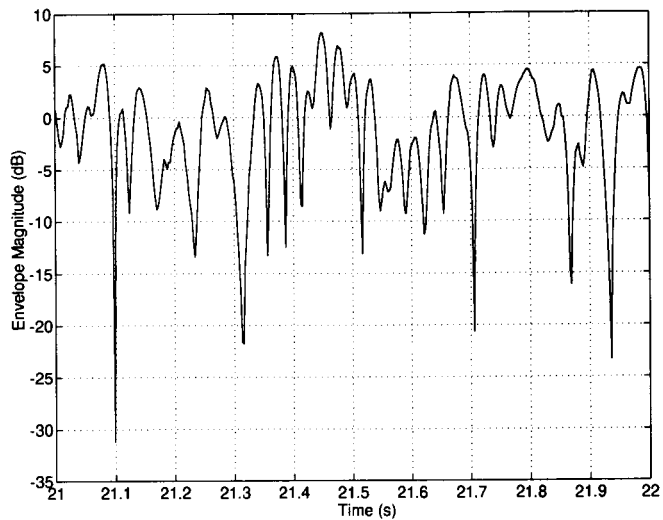### 6.3.3 Time Domain and Frequency Domain Plots


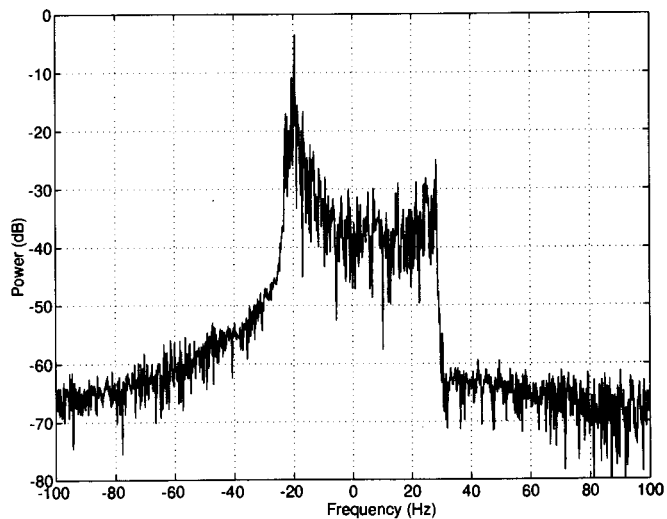
Figure 6.7: Field Fading Envelope



Figure 6.8: Field Fading Spectrum

Figure 6.7 shows the fading envelope for channel 1 for a period of 1 sec.

The fading spectrum was generated using a 10 sec block of data. The results indicated that the doppler frequency was 22Hz which corresponds to a vehicle traveling at 29.2km/hr.

The slight irregularity seen in Figure 6.8 was due to log-normal fading of the signal and acceleration of the vehicle.

Both the fading envelope and the fading spectrum match the model described in Section 2.

## 6.4 Antenna Element Correlation

### 6.4.1 Correlation Results

This section looks at the observed correlation between the different antenna elements. Observations suggest that there was far less correlation between the elements than hypothesized. Also, the correlation varies greatly in time. Since the vehicle never ventured beyond $\pm 20^{\circ}$ from boresight, the correlation results would suggest that there were some scatterers local to the base-station antenna. If this were the case, you would most definitely see the poor and varying correlation measured. It is not surprising that there were scatterers close to the base-station antenna. Because each element was omni-directional, any objects behind the antenna would act as a scatterer. There were a number of objects behind the antenna while the tests were performed. People, satellite dishes, air vents and a roof access shed all functioned as scatterers local the base-station antenna. Next time, the individual antenna elements should be directional, this way any signals reflected off scatterers behind the antenna will be attenuated and the base-station will perform much more like the model discussed earlier.

Both the envelope correlation matrix and the quadrature signal correlation matrices are shown here. The matrices are shown for two different periods in time to illustrate how the antenna element correlation varies in time due to local scatterers.

Also presented here are six plots of the envelope correlation between elements as a function of time. $\rho_{12}, \rho_{13}, \ldots, \rho_{17}$ are plotted vs. time. Notice that the correlations vary in unison; only, the further the element spacing, the more severe the variations are. This is consistent with scatterers local to the receive antenna.

For all the correlation plots and matrices, data for $\pm 0.5$s around the specified time was used to calculate the correlation coefficients.

Figure 6.21(a) shows the steering pattern for the antenna at a time when the correlation between the elements is particularly poor. The plot suggests the existence of a local scatterer at about $45^{\circ}$ from
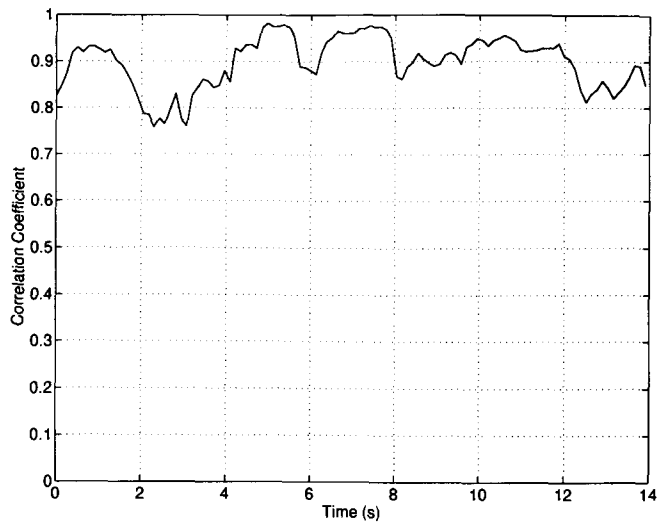
Figure 6.9: Envelope Correlation $\rho_{12}$

antenna boresight. It can be compared to Figure 6.21(b) which is a plot of the antenna pattern when the correlation between elements is good.
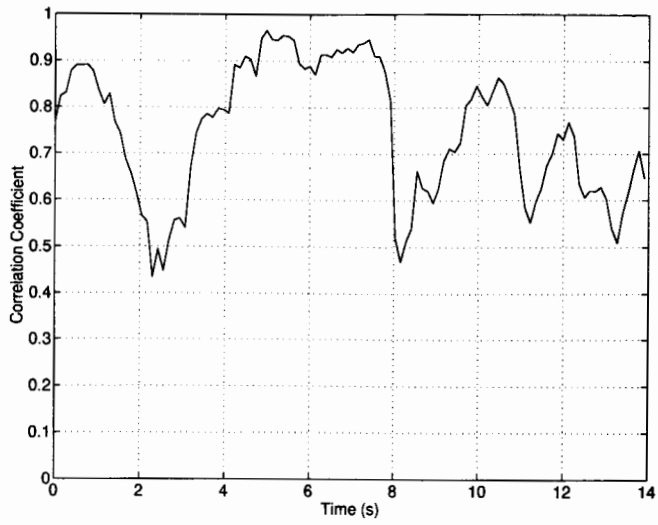
Figure 6.10: Envelope Correlation $\rho_{13}$
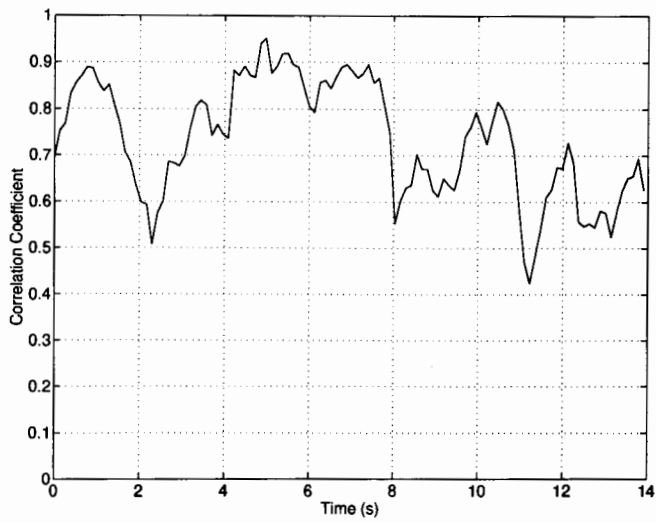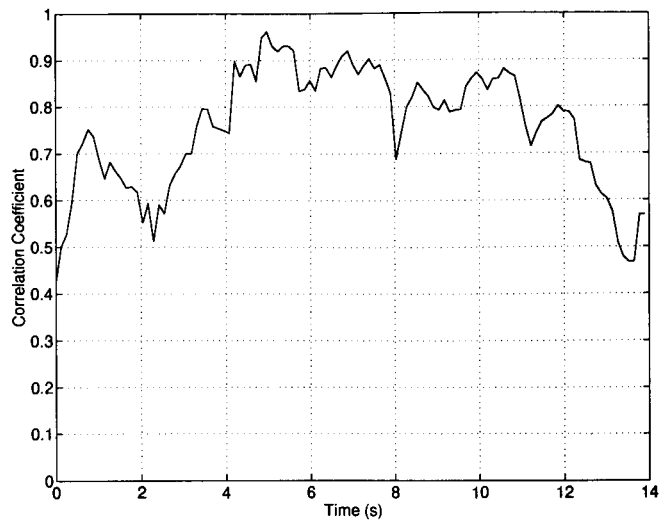


Figure 6.11: Envelope Correlation $\rho_{14}$

75

Figure 6.12: Envelope Correlation $\rho_{15}$
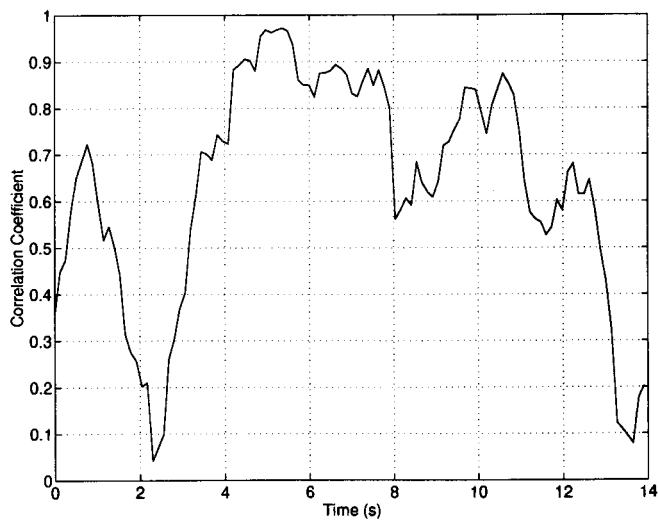


Figure 6.13: Envelope Correlation $\rho_{16}$

76
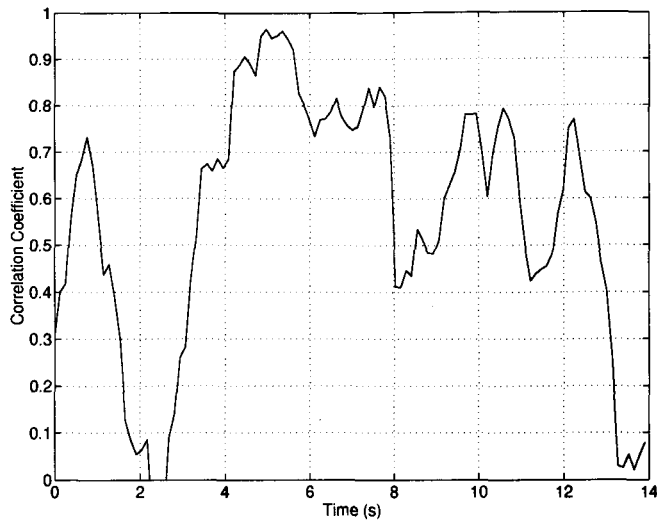
Figure 6.14: Envelope Correlation $\rho_{17}$

$$
\begin{bmatrix}
1.0000 & 0.7651 & 0.4481 & 0.6010 & 0.5714 & 0.0979 & -0.0826 \\
0.7651 & 1.0000 & 0.7539 & 0.6560 & 0.7857 & 0.4658 & 0.1931 \\
0.4481 & 0.7539 & 1.0000 & 0.7084 & 0.6282 & 0.6411 & 0.4742 \\
0.6010 & 0.6560 & 0.7084 & 1.0000 & 0.6164 & 0.5316 & 0.4439 \\
0.5714 & 0.7857 & 0.6282 & 0.6164 & 1.0000 & 0.6238 & 0.1730 \\
0.0979 & 0.4658 & 0.6411 & 0.5316 & 0.6238 & 1.0000 & 0.7371 \\
-0.0826 & 0.1931 & 0.4742 & 0.4439 & 0.1730 & 0.7371 & 1.0000
\end{bmatrix}
$$

Figure 6.15: Envelope Correlation ($t = 2.5$sec)

77

$$\begin{bmatrix} 1.0000 & 0.9293 & 0.8901 & 0.8566 & 0.7005 & 0.6493 & 0.6491 \\ 0.9293 & 1.0000 & 0.9412 & 0.9023 & 0.8161 & 0.7197 & 0.6830 \\ 0.8901 & 0.9412 & 1.0000 & 0.9322 & 0.8750 & 0.7696 & 0.7191 \\ 0.8566 & 0.9023 & 0.9322 & 1.0000 & 0.8933 & 0.8575 & 0.8069 \\ 0.7005 & 0.8161 & 0.8750 & 0.8933 & 1.0000 & 0.9023 & 0.8139 \\ 0.6493 & 0.7197 & 0.7696 & 0.8575 & 0.9023 & 1.0000 & 0.9395 \\ 0.6491 & 0.6830 & 0.7191 & 0.8069 & 0.8139 & 0.9395 & 1.0000 \end{bmatrix}$$

Figure 6.16: Envelope Correlation ($t = 0.5$sec)

$$\begin{bmatrix} 1.0000 & 0.9052 & 0.7846 & 0.8482 & 0.8508 & 0.6352 & 0.4588 \\ 0.9052 & 1.0000 & 0.9275 & 0.8997 & 0.9341 & 0.8149 & 0.6666 \\ 0.7846 & 0.9275 & 1.0000 & 0.9108 & 0.8612 & 0.8754 & 0.7776 \\ 0.8482 & 0.8997 & 0.9108 & 1.0000 & 0.8501 & 0.7997 & 0.7104 \\ 0.8508 & 0.9341 & 0.8612 & 0.8501 & 1.0000 & 0.8794 & 0.6306 \\ 0.6352 & 0.8149 & 0.8754 & 0.7997 & 0.8794 & 1.0000 & 0.8865 \\ 0.4588 & 0.6666 & 0.7776 & 0.7104 & 0.6306 & 0.8865 & 1.0000 \end{bmatrix}$$

Figure 6.17: I Correlation ($t = 2.5$sec)

$$\begin{bmatrix} 1.0000 & 0.9063 & 0.7434 & 0.8236 & 0.8216 & 0.6029 & 0.3561 \\ 0.9063 & 1.0000 & 0.8926 & 0.8636 & 0.9162 & 0.7981 & 0.5735 \\ 0.7434 & 0.8926 & 1.0000 & 0.8786 & 0.8624 & 0.8667 & 0.7788 \\ 0.8236 & 0.8636 & 0.8786 & 1.0000 & 0.8701 & 0.8039 & 0.7491 \\ 0.8216 & 0.9162 & 0.8624 & 0.8701 & 1.0000 & 0.8689 & 0.6757 \\ 0.6029 & 0.7981 & 0.8667 & 0.8039 & 0.8689 & 1.0000 & 0.9046 \\ 0.3561 & 0.5735 & 0.7788 & 0.7491 & 0.6757 & 0.9046 & 1.0000 \end{bmatrix}$$

Figure 6.18: Q Correlation ($t = 2.5$sec)

$$\begin{bmatrix} 1.0000 & 0.9780 & 0.9658 & 0.9440 & 0.8956 & 0.8929 & 0.8867 \\ 0.9780 & 1.0000 & 0.9814 & 0.9577 & 0.9369 & 0.9130 & 0.8834 \\ 0.9658 & 0.9814 & 1.0000 & 0.9707 & 0.9566 & 0.9222 & 0.8901 \\ 0.9440 & 0.9577 & 0.9707 & 1.0000 & 0.9598 & 0.9388 & 0.8999 \\ 0.8956 & 0.9369 & 0.9566 & 0.9598 & 1.0000 & 0.9525 & 0.9054 \\ 0.8929 & 0.9130 & 0.9222 & 0.9388 & 0.9525 & 1.0000 & 0.9758 \\ 0.8867 & 0.8834 & 0.8901 & 0.8999 & 0.9054 & 0.9758 & 1.0000 \end{bmatrix}$$

Figure 6.19: I Correlation ($t = 0.5$sec)

$$\begin{bmatrix} 1.0000 & 0.9727 & 0.9499 & 0.9210 & 0.8574 & 0.8118 & 0.8100 \\ 0.9727 & 1.0000 & 0.9731 & 0.9539 & 0.9236 & 0.8816 & 0.8631 \\ 0.9499 & 0.9731 & 1.0000 & 0.9639 & 0.9461 & 0.8967 & 0.8812 \\ 0.9210 & 0.9539 & 0.9639 & 1.0000 & 0.9567 & 0.9459 & 0.9306 \\ 0.8574 & 0.9236 & 0.9461 & 0.9567 & 1.0000 & 0.9741 & 0.9443 \\ 0.8118 & 0.8816 & 0.8967 & 0.9459 & 0.9741 & 1.0000 & 0.9798 \\ 0.8100 & 0.8631 & 0.8812 & 0.9306 & 0.9443 & 0.9798 & 1.0000 \end{bmatrix}$$

Figure 6.20: Q Correlation ($t = 0.5$sec)
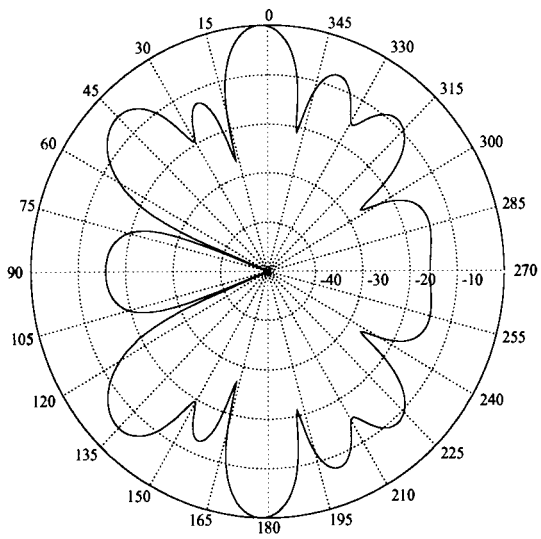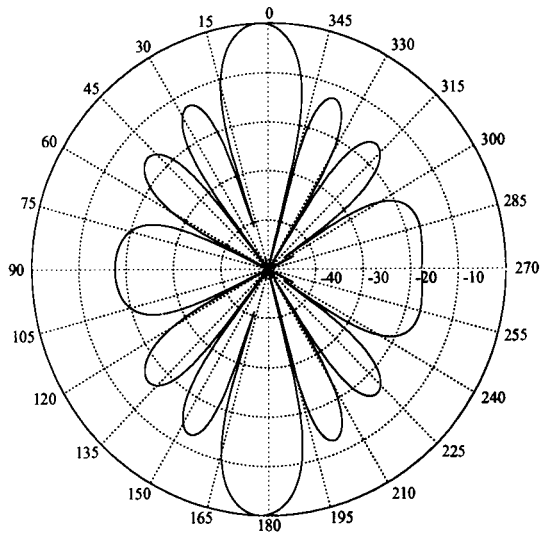
(a)                                    (b)

Figure 6.21: Antenna Steering Pattern During Poor Element Correlation

## 6.4.2 Explanation of Correlation Results

As mentioned above, the correlations dip periodically which is consistent with having scatterers local to the receive antenna. To prove this was the case, simulations were done to demonstrate the periodic degradation in signal correlation between antenna elements. Figure 6.22 shows the model used in the simulations. A vehicle 2 km from the antenna array and traveling at 20 km/hr generated a Rayleigh fading signal. A single scatterer was placed at the position shown (roughly $45^o$ from boresight) and it was assumed the signal reflected off the scatterer was 3dB below the direct signal. The vehicle started at $7^o$ left of boresight and traveled along the indicated path for 14 seconds. As the vehicle moved, the signals received by the two antennas were calculated. The same algorithm used in the previous section was used again to calculate the correlation between elements over time. The results can be seen in Figures 6.23 and 6.24.

The simulated results show the same periodic dips in correlation seen in the field test results. The severity of the dips is dependent on the geometry of the situation and the relative strength of the reflected signal so an exact match between the field tests and simulations is difficult. But, the simulations backup the theory that the dips observed in the field tests were the result of a scatterer near the receive antenna array.
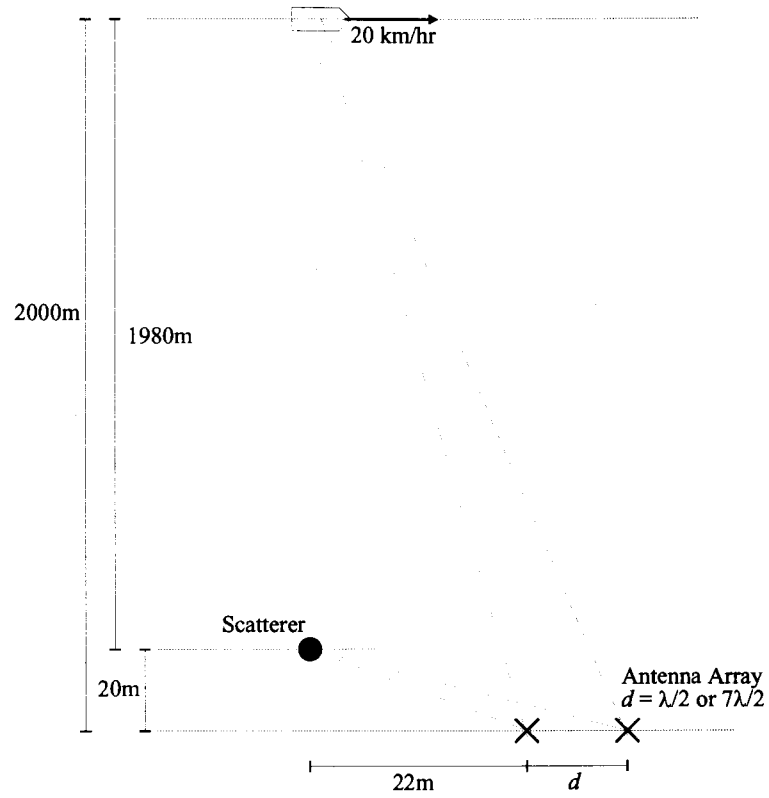
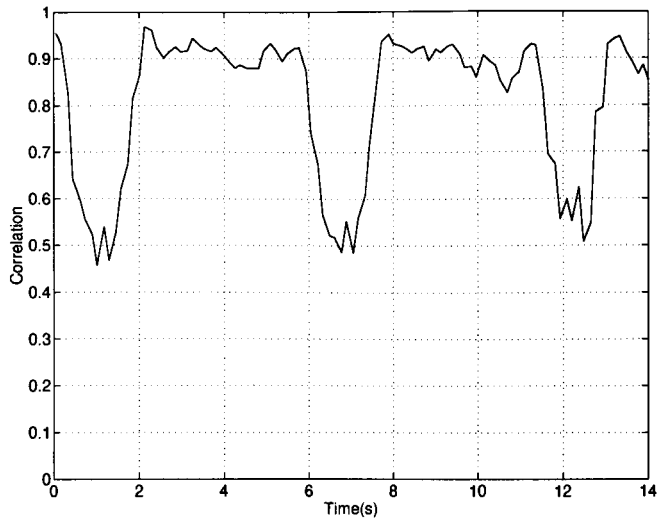Figure 6.22: Model for Correlation Simulations
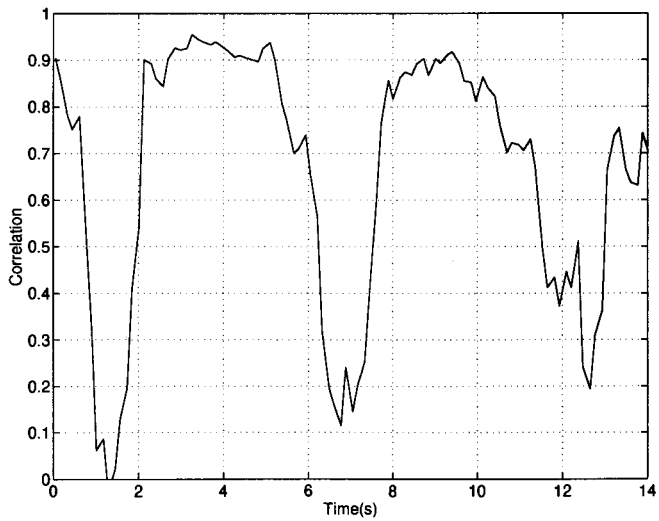
Figure 6.23: Theoretical Envelope Correlation $\rho_{12}$



Figure 6.24: Theoretical Envelope Correlation $\rho_{17}$

83

## 6.5 Vehicle Tracking

This section looks at tracking the vehicle as it moves through the environment. Figures 6.25(a) and 6.26(a) show the antennas steering pattern at two different time periods during the field tests. Notice that the major lobe in the steering pattern has changed by about $10^o$ suggesting that the vehicle has traversed a $10^o$ angle in front of the receiving antenna. The patterns also closely match the theoretical patterns shown in Figures 6.25(b) and 6.26(b).

Figure 6.27 shows the calculated vehicle angle as a function of time. An algorithm, which steers the beam through $360^o$ and records the angle where the signal strength was the strongest, was used to track the vehicle. Using this very simple tacking algorithm, the antenna was the able to follow the vehicle as it moved through the environment. Refer to [4] for more information on the tracking algorithm used.
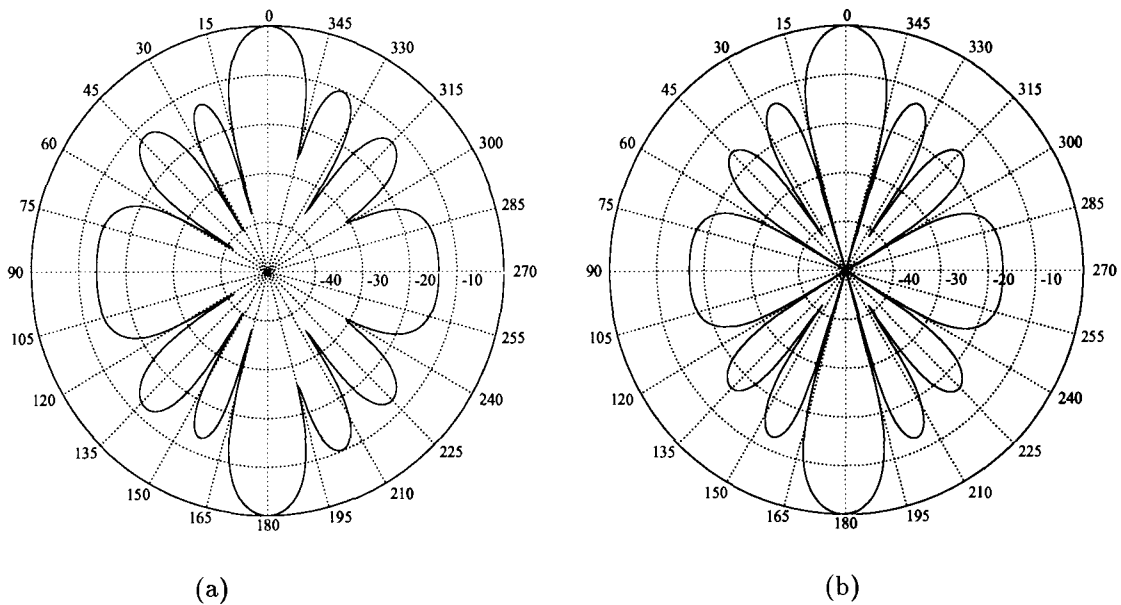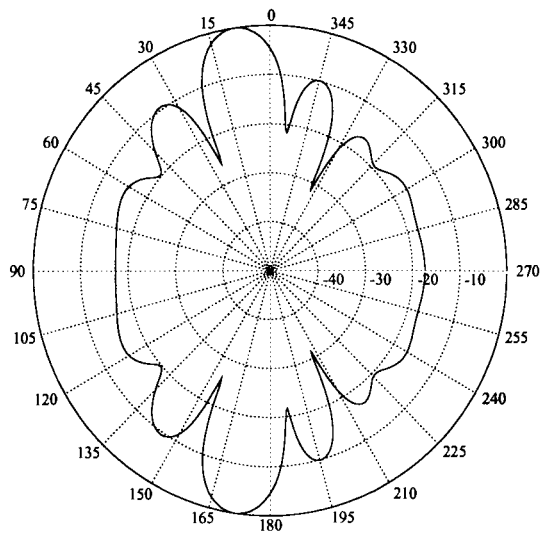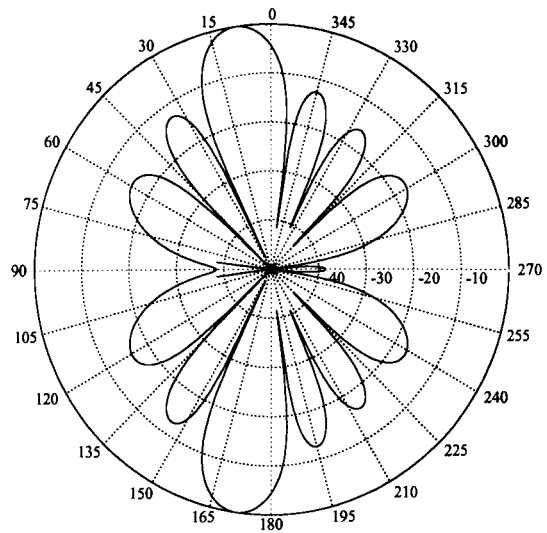


(a)  (b)

Figure 6.25: Vehicle Angle Detection – Vehicle at $0^o$

(a)                                    (b)

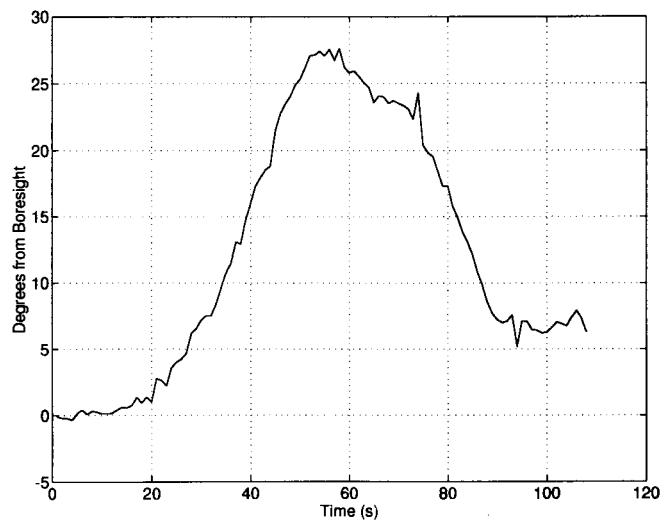Figure 6.26: Vehicle Angle Detection – Vehicle at 10°



Figure 6.27: Vehicle Tracking

# Chapter 7

# conclusions

## 7.1   The Spatial Channel Simulator

The designer of any mobile communications system knows that field tests are an inevitable procedure necessary in determining a systems true performance. It is time consuming, expensive and often inconclusive due to uncertainty in the statistical signal variations actually encountered. Laboratory testing using special equipment designed to simulate the statistical properties of the signals encountered in the field is an attractive alternative. Fading channel simulators have existed for a number of years, but proposals for multi-element directional base-stations has sparked an interest in spatial channel simulators.

The spatial channel simulator presented here performs exceptionally well at simulating the fading environment. There are no know spatial channel simulators available on the market, so one has to look at existing fading channel simulators for a performance comparison. Most fading channel simulators employ analog techniques to generate $I$ and $Q$ and shape the RF spectrum. The DSP approach presented in this thesis far surpasses the performance offered by the analog equivalents. A DSP based simulator is particularly good at recreating the RF fading spectrum as seen in Figure 4.6. The RF fading spectrum generated by the spatial channel simulator agrees very closely to theory and that measured in the field.

Another strength of the spatial channel simulator presented in this thesis can be seen by comparing Figures 3.3 and 4.9. The agreement between the correlation programmed into the DSP and that measured on the outputs of the spatial channel simulator was exceptional. Using a DSP in the simulator's design permitted very precise control over the correlations observed between simulator outputs.

The probability distribution functions (PDFs) for the signal magnitude and phase between $I$ and $Q$ are also in close agreement to theory and that measured in the field.

It's true, the spatial channel simulator was simplified to make its implementation easier, but these simplifications, which are summarized below, are either well justified or obvious extensions of the existing system.

- The spatial channel simulator developed for this project, like most simulators, ignores the delay spread effect on the transmitted signal. Delay spread can only be accounted for using a number of expensive RF delay lines and summing their output. Also, delay spread only becomes noticeable as the bandwidth of the transmitted signal $B_s$ approaches the coherence bandwidth of the environment ($B_c = \frac{1}{2\pi\Delta}$ where $\Delta$ = delay spread). In our case $B_s = 5kHz << B_c = 636kHz$ (delay spread $\Delta = 0.25\mu s$).

- The simulator does not take into account co-channel interference. It is something which is possible to include, but every interferer included would require full duplication of the RF hardware in the SCS. The same DSP could be used to control both the desired signal and all the interferers. But, because each source's position relative to the receive antenna is different and because the fading characteristics of the signals from the different sources are independent, they would each require separate I-Q modulators.

- The mobiles position was restricted to $\pm 20^o$ from boresight. Considering the communications system described in Section 3.2, this is a valid restriction. However, for a general communications system, the simulator should allow for any vehicle position.

- The simulator does not recreate log-normal fading. Log-normal fading is a simple feature to include and unnecessarily complicated the analysis of the simulator.

The major problem encountered with the design of the simulator was computing capability. A TI 'C30 floating point DSP processor was used. But, even its capability was being over extended due to the number of computations involved. The simulation results seen in Section 4.3.3 were generated with the DSP running as fast as possible. Figure 4.6 shows that maximum computing speed translates into an $f_m$ of only 20Hz or a vehicle speed of 27 km/h. I don't see this as a problem because all the code for the DSP was written in 'C' and no care was taken to optimize the execution speed. Even the spectral shaping filter was written in 'C' with floating point taps. Since about 80% of the processing time was spent in this routine, re-writing it in assembler using integer taps would provide a speed increase of about $5\times$. As a proof of concept, the simulator performed very well, but work will have to be done to increase its speed before it can be used as a simulator in the lab.

## 7.2   The Phased Array Antenna

The results of the field tests alone are very significant. Fading data with reference to a multi-element base-station has never been gathered and recorded in such a manner before. Each of the antenna's signals was demodulated to two complex base band signals and the samples recorded on CD. This not only allowed the analysis presented here to be done in leisure, but it also allowed for great flexibility in future analysis of the data. Such things as beam steering algorithms, angle diversity algorithms, null steering algorithms, etc. are being investigated and their performance evaluated [14] [4].

As Figure 6.25(a) shows, the antenna array functioned very well. Comparing Figure 6.25(a) to Figure 6.25(b) shows the measured antenna array pattern was almost identical the theoretical pattern.

The PDF for the signal envelope, the PDF for the $I$ and $Q$ phase distribution, the envelope level crossing rate and the RF fading spectrum measured in the field all agree closely to the theoretical performance

derived in Section 2.3. This is a very important result because it means the model developed in Section 2.3 is very good for predicting the signal received by a base-station directional antenna and can be used in future simulations investigating other aspects of directional base-station antennas employed in the mobile environment.

Unfortunately, the correlation measured between the elements of the phased array antenna was tainted by scatterers local to the receive antenna. As shown in Figure 3.1 and discussed in Section 2.3, the correlation between the elements should have been very close to 1 and not change with arrival angle when the arrival angle is restricted to boresight $\pm 20^o$. The results shown in Figures 6.9 through 6.20 indicate that the correlation measured in the field did vary greatly with the vehicles position with the correlations falling near zero at times. Scatterers local to the receive antenna were the reason for the discrepancy between theory and the measured results. In fact, Figure 6.21 verifies the existence of a local scatterer at about $115^o$ from antenna boresight.

It was not surprising that the results show the effects of scatterers close to the base-station antenna. Because each element was omni-directional, any object behind the antenna acted as a scatterer. There were a number of objects behind the antenna as seen in Figures 5.12 and 5.13. People, satellite dishes, air vents and a roof access shed all functioned as scatterers local to the base-station antenna. Next time, the individual antenna elements should be directional, this way any signals reflected off scatterers behind the antenna will be attenuated and the base-station will perform much more like the model discussed in Section 2.3.

# Bibliography

[1] Gaston A. Arredondo, William H. Chriss, and Edward H. Walker. A multipath fading simulator for mobile radio. *IEEE Transactions on Vehicular Technology*, VT-22(4):241–244, November 1973.

[2] R. Ball. A real-time fading simulator for mobile radio. *The Radio and Electronic Engineer*, 52(10):475–478, October 1982.

[3] Edgar L. Caples, Khalil E. Massad, and Timothy R. Minor. A uhf channel simulator for digital mobile radio. *IEEE Transactions on Vehicular Technology*, VT-29(2):241–244, May 1980.

[4] Xavier Carbo. Tracking and diversity for a mobile communications base-station array antenna. Master's thesis, Simon Fraser University – School of Engineering Science, August 1995.

[5] Faramaz Davarian. Channel simulation to facilitate mobile-satellite communications research. *IEEE Transactions on Communications*, COM-35(1):47–56, January 1987.

[6] Faramez Davarian. Hardware simulator assists mobile satellite experiment. In *IEEE 35th Vehicular Technology Conference*, pages 1–8, May 1985.

[7] William C. Jr. Jakes. *Microwave Mobile Communications*. John Wiley & Sons Inc., New York, London, Sydney, Toronto, 1974.

[8] William C.Y. Lee. Effects on correlation between two mobile radio base-station antennas. *IEEE Transactions on Communications*, COM-21(11):1214–1224, November 1973.

[9] William C.Y. Lee. *Mobile Communications Engineering.* McGraw-Hill Book Company, New York, St. Louis, San Francisco, Toronto, 1982.

[10] William H. Press, Saul A. Teukolsky, William T. Vetterling, and Brian P. Flannery. *Numerical Recipes in C – The Art of Scientific Computing Second Edition.* Cambridge University Press, New York, 1992.

[11] Sam K. Shanmugan and Arthur M. Breipohl. *Random Signals: Detection, Estimation and Data Analysis.* John Wiley & Sons Inc., New York, London, Sydney, Toronto, 1988.

[12] Shawn P. Stapleton, Xavier Carbo, and Trent O. McKeen. Spatial channel simulator for phased arrays. In *IEEE 44th Vehicular Technology Conference,* pages 1789–1792, June 8–10 1994.

[13] Shawn P. Stapleton and G.S. Quon. A cellular base station phased array antenna system. In *IEEE 43th Vehicular Technology Conference,* pages 1789–1792, June 8–10 1993.

[14] Sarkis Teghararian. Interference rejection for a mobile communications array antenna. Master's thesis, Simon Fraser University – School of Engineering Science, August 1995.